Design of Optical and Radiative Properties of Surfaces

Bo Zhao and Zhuomin M. Zhang

Abstract

Tailoring optical and radiative properties has attracted a great deal of attention in recent years due to its importance in advanced energy systems, nanophotonics, electro-optics, and nanomanufacturing. Micro-/nanostructured surfaces can interact with electromagnetic waves in a unique way by excitation of various optical resonances or polaritons that can modify the polarization-dependent directional and spectral radiative properties. Latest advances in graphene and other two-dimensional (2D) materials offer enormous potentials to revolutionize current microelectronic, optoelectronic, and energy harvesting systems. This chapter summarizes the recent advances in the design of optical and radiative properties of micro-/nanostructures and 2D materials. The physical mechanisms that are behind the exotic behaviors are discussed, with an emphasis on various plasmonic and phononic polaritons. Anisotropic rigorous coupled-wave analysis is presented as a modeling technique that is suitable to simulate periodic multilayer structures involving anisotropic materials. The insights gained from this chapter may benefit the future development of energy harvesting systems, photodetectors, thermal management, local thermal management, and high-resolution thermal sensing.

Contents

B. Zhao • Z.M. Zhang (✉)
George W. Woodruff School of Mechanical Engineering, Georgia Institute of Technology, Atlanta, GA, USA
e-mail: bzhao35@gatech.edu; zhuomin.zhang@me.gatech.edu

F.A. Kulacki (ed.), *Handbook of Thermal Science and Engineering*,
DOI 10.1007/978-3-319-32003-8_58-1

1 Introduction

Radiation from a thermal source, such as an incandescent light bulb, is usually incoherent. However, in the late 1990s and at the beginning of the twenty-first century, researchers demonstrated that the thermal radiation from a periodically patterned grating surface with a period smaller than the typical wavelength of the thermal radiation can be coherent (to certain degree) in narrow wavelength bands as well as in a well-defined direction (Hesketh et al. 1986; Greffet et al. 2002). Since then, various subwavelength micro-/nanostructures have been proposed that can tailor optical and radiative properties both spectrally and directionally (Lee et al. 2005; Dahan et al. 2008; Cai and Shalaev 2009; Tan et al. 2016). This research area has gained increasing attention due to the widespread important applications (Zhang et al. 2003; Zhang 2007), such as photodetectors (Chang et al. 2010; Kulkarni et al. 2010; Li and Valentine 2014), band-pass filters (Ebbesen et al. 1998; Porto et al. 1999; Baida and Van Labeke 2002; Lee et al. 2008a), negative refraction (Pendry 2000; Shelby et al. 2001; Smith et al. 2004; Shalaev et al. 2005), anomalous reflection (Grady et al. 2013; Hou-Tong et al. 2016), clocking (Pendry et al. 2006; Schurig et al. 2006; Cai et al. 2007; Liu et al. 2009), surface-enhanced Raman spectroscopy (Stiles et al. 2008), medical therapy (Cai et al. 2008), thermo-photovoltaics (TPV) emitter and absorber (Basu et al. 2007; Wang and Zhang 2012b; Watts et al. 2012; Boriskina et al. 2013), photovoltaic and solar thermal technology (Baxter et al. 2009; Atwater and Polman 2010; Cui et al. 2012; Fan 2014; Khodasevych et al. 2015), structural color printing (Cheng et al. 2015), as well as radiative cooling (Raman et al. 2014). Tailoring radiative properties generally relies on various resonance modes or surface waves in periodic micro-/nanostructures. Among them are gratings that support surface phonon polaritons (SPhPs) (Greffet et al. 2002) or surface plasmon polaritons (SPPs) (Raether 1988; Zayats et al. 2005; Williams et al. 2008), hyperbolic metamaterials that can empower hyperbolic modes and epsilon-near-zero modes (Krishnamoorthy et al. 2012; Poddubny et al. 2013; Othman et al. 2013), and metal/dielectric/metal structures and deep gratings that can enable magnetic polaritons (MPs) (Lee et al. 2008b; Zhao and Zhang 2014; Xuan and Zhang 2014). Meanwhile, various structures like photonic crystals (Luo et al. 2004), nanowire arrays (Zhang and Ye 2012), and nanoparticles (Didari and Menguc 2015) have also been extensively studied for their radiative properties. Figure 1 shows various metal/dielectric/metal structures that can support MPs from visible to far-infrared region (Sakurai et al. 2014). The radiative properties of rough surfaces

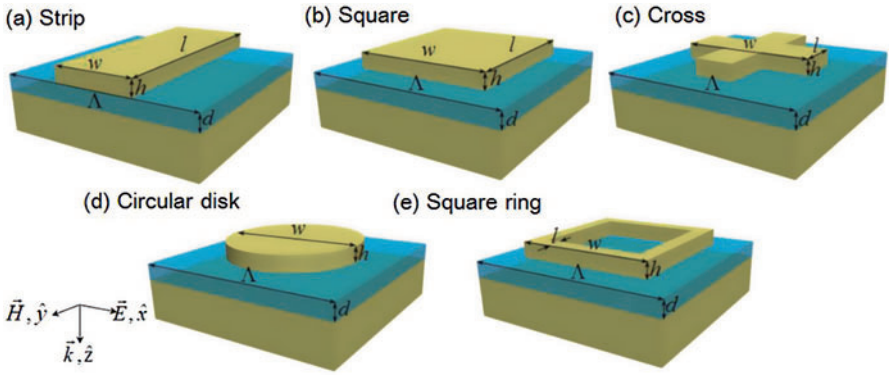

Fig. 1 Schematic of metal/dielectric/metal emitters and absorbers with different top metal patterns over a ground plate separated by a dielectric spacer: (**a**) strip, (**b**) square, (**c**) cross, (**d**) circular disk, and (**e**) square ring. The geometry factors are illustrated in the figure (From Sakurai et al. 2014)

have been investigated and reviewed (Zhu et al. 2009). The optical and radiative properties of these period micro-/nanostructured surfaces can be dramatically different from the radiative properties of the counterpart rough or smooth surfaces due to the excitation of surface waves and polaritons.

Emerging two-dimensional (2D) materials (Geim and Grigorieva 2013; Xia et al. 2014), including graphene (Novoselov et al. 2004; Lin and Connell 2012; Grigorenko et al. 2012; Koppens et al. 2014; Bonaccorso et al. 2015), hexagonal boron nitride (hBN) (Dai et al. 2014), transition metal dichalcogenides (Wang et al. 2015), and recently emerged black phosphors (Ling et al. 2015), offer exciting new possibilities to construct micro-/nanostructures with unprecedented optical and radiative properties. With a layer of carbon atoms arranged in a honeycomb lattice, graphene exhibits unique electronic, thermal, mechanical, and optical properties (Nair et al. 2008; Thongrattanasiri et al. 2012; Pop et al. 2012). It enables saturation absorption in the visible and near-infrared region, and low-loss, actively tunable surface plasmons in mid- and far-infrared region (Novoselov et al. 2004; Grigorenko et al. 2012; Nair et al. 2008), which have been demonstrated for their ability to control thermal radiation (Freitag et al. 2010). Hyperbolic 2D materials like hBN (Lin and Connell 2012; Dai et al. 2014, 2015b; Brar et al. 2014; Kumar et al. 2015) can support plentiful phononic resonance modes with unique radiative properties. Moreover, it is recently demonstrated that 2D materials can be used together with nano-/microstructures to assemble hybrid structures with unique tunable radiative properties by enabling plentiful coupling effects (Li et al. 2016).

Optical and radiative properties essentially describe the way that light interacts with matters (▶ Introduction: Thermal Radiation Heat Transfer). When the characteristic length of the material or structure is much longer than the wavelength of light, the polarization and vector attributes of light may be neglected, and radiative properties of this scale can be solved using ray tracing or geometrical optics (Modest 2013; Howell et al. 2015). However, to calculate the radiative properties of

subwavelength periodic nano-/microstructured surfaces, Maxwell's equations have to be solved to fully consider the vector and polarization characters of electromagnetic waves (Zhang et al. 2003; Xuan 2014; ▶ Heat Transfer Physics: From Nano- to Macro-Scales). Recent advances in 2D materials put new challenges on the numerical modeling of the optical and radiative properties due to their atomically thin thickness and natural anisotropy, especially when 2D materials are combined with periodic nanostructures.

This chapter is intended to discuss the numerical modeling of periodic micro-/nanostructures and different 2D materials, as well as the unique optical and radiative properties of typical subwavelength structures. An anisotropic rigorous coupled-wave analysis (RCWA) algorithm is described that can be used to model multilayer periodic micro-/nanostructures involving anisotropic materials. Optical and radiative properties of different micro-/nanostructures, 2D materials, as well as various hybrid structures are reviewed with their potential applications. The physical mechanisms of the unique radiative properties are discussed. The arrangement of this chapter is listed in the following:

Section 2 discusses the popular modeling techniques, with a focus on anisotropic RCWA. The basics are summarized with equations emphasizing the difference as compared to the original RCWA. The fundamentals of light diffraction by periodic structured surfaces are discussed to serve as the theoretical background. The optical and radiative properties micro-/nanostructures are reviewed, including the underlying mechanism of MPs in deep gratings, the radiative properties of SPPs in 2D nanostructures, and anisotropic metamaterials.

Section 3 reviews the potential applications of tailored thermal radiative properties with an emphasis on the application of TPVs.

Section 4 summarizes the recent research on using 2D materials with nanostructures to achieve unique radiative properties. Wavelength-selective perfect absorption in graphene and hBN-covered metal gratins are specifically discussed. The underlying mechanisms are discussed with an emphasis on the role of 2D materials in modifying the radiative properties of nano-/microstructures.

2 Modeling and Theoretical Fundamentals of Periodic Structures

2.1 Numerical Methods for Modeling Optical Properties of Period Structures

Maxwell's equations describe how electromagnetic waves propagate in a certain medium and interact with objects in the medium. Together with the constitutive relations from which the permittivity and permeability of the medium can be obtained, radiative properties can be attained by studying how light interacts with various objects. Numerical methods are usually used to simulate the radiative properties of periodic structures since analytical solutions are seldom available due to the complex geometries (Xuan 2014). Computational electromagnetics models

the interaction of electromagnetic fields with physical objects and the environment. It is widely used to calculate antenna performance, radar cross section, and electromagnetic wave propagation in a certain medium or structure. Various computational techniques have been developed. Choosing the right technique for solving a certain problem is important, because using an inappropriate one may make the computational time excessively long or even lead to incorrect results. For periodic structures, the most popular simulation tools are the finite-difference time-domain (FDTD) or Yee's method (Kane 1966; Taflove and Hagness 2005), the finite-element method (FEM) (Davidson 2010), and the rigorous coupled-wave analysis (RCWA) method (Moharam and Gaylord 1981). FDTD is a time-domain method that uses wideband sources and computes a wideband response in one run, whereas RCWA is a frequency-domain method that has to calculate the system response for each frequency point. If only a narrowband response is of the interest, a very large number of time steps may be required for FDTD (Davidson 2010). Meanwhile, the properties of the material (namely, the permittivity and permeability) can be expediently expressed as a function of the frequency in the frequency domain, but it is more challenging in the time domain since a convolution is implied (Xuan 2014). FEM can be used in both time and frequency domain. All three methods are widely used. Commercial software such as Remcom XFDTD and Lumerical FDTD solutions, as well as a free-software package (Oskooi et al. 2010), are based on FDTD. COMSOL RF module and Ansoft HFSS are examples that use FEM, while RCWA programs are also accessible online free of charge (Liu and Fan 2012; Zhang 2014).

FDTD and FEM methods discretize the structure or computation domain with mesh or grid and numerically solve the quantity of interest associated with each element or cell. For structures with small dimensions like 2D materials, accrete simulation using FEM and FDTD may become very challenging and time-consuming since the dimension of the mesh needs to be very small in the out-of-plane direction, especially when structures with small characteristic lengths coexist with large structures, like the hybrid structures with 2D materials and micro-/nanostructures. On the contrary, RCWA is a semi-analytical method that does not require a discretization of the structure. Instead, the electric or magnetic field in the structure is expressed as a Fourier series with the coefficients to be solved using boundary conditions. Since mesh is not needed, RCWA has advantages in modeling the structures that contain extremely small geometries.

2.2 Anisotropic Rigorous Coupled-Wave Analysis

RCWA has been widely used in modeling the radiative properties of periodic structures. Most available RCWA algorithms are for isotropic materials based on the widely used algorithms for one-dimensional (1D) grating proposed by Moharam and Gaylord (1981). Afterward, anisotropic RCWA has been studied by different researchers. Glytsis and Gaylord (1990) formulated RCWA for 1D anisotropic gratings, but the algorithm may have convergence issues for highly conducting metal gratings because of the way that Fourier factorizations were calculated.

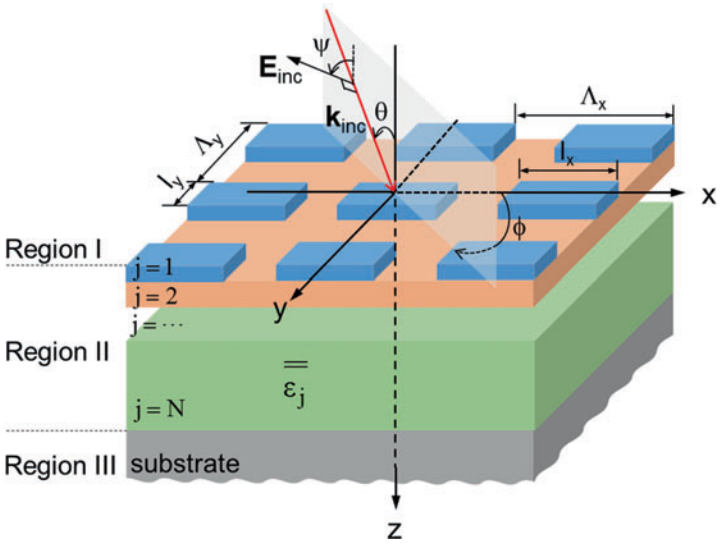

Fig. 2 Illustration of the numerical model for general 2D periodic multilayer structures consisting of anisotropic materials (From Zhao and Zhang 2016)

Later, Li (1996, 1998) reformulated the algorithm with the correct Fourier factorization rules. Continuous effort has been devoted and more general algorithms have been formulated to consider 2D arbitrary lattice configurations and permittivity tensor (Popov and Nevière 2001; Lin et al. 2002; Li 2003). In the rest of this section, an easy-to-implement algorithm to model a 2D multilayered periodic structure made of biaxial materials with a diagonal permittivity tensor is summarized. This algorithm is an extension of the public available RCWA code (Zhang 2014), and the core equations are summarized below and compared to the original RCWA, which has been presented in other works (Lee et al. 2008a; Zhang and Wang 2013; Chen and Tan 2010; Bräuer and Bryngdahl 1993). It also serves as a theoretical background of the later sections since the resonance mechanisms are easier to be understood in the frequency domain.

The 2D anisotropic multilayered periodic structure is schematically shown in Fig. 2. The periodicity is characterized by Λ_x and Λ_y, which are the periods in the x- and y-directions, respectively. Each layer in the structure can be either a grating or a continuous film by adjusting the lateral dimensions l_x and l_y. In the schematic, the first layer is a 2D grating and the rest are films. The medium where the wave is incident, the intermediate layers (total N layers), and the semi-infinite substrate can be categorized as Region I, II, and III, respectively, as indicated in the schematic. The incident medium with a dielectric function ε_I is usually vacuum or lossless dielectric and set to be isotropic. The incident wave with an electric field $\mathbf{E}_{\text{inc}}$ is assumed to be linearly polarized. The plane of incidence indicated in transparent gray color is the plane determined by the incident wave vector $\mathbf{k}_{\text{inc}} = (k_{x,\text{ inc}}, k_{y,\text{ inc}}, k_{z,\text{ inc}})$ and the z-axis. A polar angle θ (the angle between $\mathbf{k}_{\text{inc}}$ and the z-axis) and

azimuthal angle ϕ (the angle between the x-axis and the plane of incidence) are used to depict the direction of $\mathbf{k}_{\text{inc}}$. Polarization angle ψ is defined as the angle between the electric field and the plane of incidence.

In Region I, the electric field contains the incident and reflected fields and the expression is the same as the isotropic RCWA (Zhao et al. 2013):

$$\begin{aligned}\mathbf{E}_{\text{I}} = \mathbf{E}_{\text{inc}} \exp\left(i\mathrm{k}_{x,\text{inc}} x + i\mathrm{k}_{y,\text{inc}} y + i\mathrm{k}_{z,\text{inc}} z\right) \\ + \sum_m \sum_n \mathbf{E}^r_{mn} \exp\left(i\mathrm{k}_{x,m} x + i\mathrm{k}_{y,n} y - i\mathrm{k}^r_{z,mn} z\right)\end{aligned} \tag{1}$$

The time-harmonic term, $\exp(-i\omega t)$, with ω being the angular frequency, is omitted hereafter. The second term on the right-hand side is the reflected wave. $\mathbf{E}^r_{mn}$ is the complex amplitude of the (m, n) order reflected wave, and its transverse wave vector components are determined by the Bloch-Floquet condition (Glytsis and Gaylord 1990):

$$\begin{aligned}k_{x,m} &= k_{x,\text{inc}} + m\frac{2\pi}{\Lambda_x} \\ k_{y,n} &= k_{y,\text{inc}} + n\frac{2\pi}{\Lambda_y}\end{aligned} \tag{2}$$

where m and n denote the diffraction orders in the x- and y-directions, respectively, and they can take both positive and negative numbers. The z-components of the wave vector is

$$k^r_{z,mn} = \begin{cases} \sqrt{k_{\text{I}}^2 - k_{x,m}^2 - k_{y,n}^2} & , \quad \varepsilon_{\text{I}} k_0^2 \geq k_{x,m}^2 + k_{y,n}^2 \\ i\sqrt{k_{x,m}^2 + k_{y,n}^2 - k_{\text{I}}^2} & , \quad \varepsilon_{\text{I}} k_0^2 < k_{x,m}^2 + k_{y,n}^2 \end{cases} \tag{3}$$

where $k_0 = \omega/c_0$ is the wave vector (magnitude) in vacuum with c_0 being the speed of light in vacuum.

In each layer of Region II, both the electromagnetic field and the dielectric function are expressed as Fourier series based on the periods in the x- and y-directions. The materials of each layer are assumed to be nonmagnetic, and thus the dielectric function of the layer can be described by a location-dependent permittivity tensor:

$$\overline{\overline{\varepsilon_j}}(x, y) = \begin{pmatrix} \varepsilon_{j,x} & 0 & 0 \\ 0 & \varepsilon_{j,y} & 0 \\ 0 & 0 & \varepsilon_{j,z} \end{pmatrix} \tag{4}$$

where j is the number of the layer in the structure ranging from 1 to N. Generally, $\varepsilon = \varepsilon' + i\varepsilon''$ is a complex number with ε' and ε'' being its real and imaginary part, respectively. The electric and magnetic field can be expressed as

$$\begin{aligned}\mathbf{E}_{\mathrm{II}} &= \sum_m \sum_n \chi_{mn}(z)\exp\left(ik_{x,m}x + ik_{y,n}y\right)\\ \mathbf{H}_{\mathrm{II}} &= i\sqrt{\frac{\varepsilon_0}{\mu_0}}\sum_m \sum_n \gamma_{mn}(z)\exp\left(ik_{x,m}x + ik_{y,n}y\right)\end{aligned} \tag{5}$$

The unknowns $\chi_{mn}(z)$ and $\gamma_{mn}(z)$ can be related by the following equations based on Maxwell's equations, $\nabla \times \mathbf{E}_{\mathrm{II}} - i\omega\mu_0\mathbf{H}_{\mathrm{II}} = 0$ and $\nabla \times \mathbf{H}_{\mathrm{II}} + i\omega\varepsilon_0\bar{\bar{\varepsilon}}\mathbf{E}_{\mathrm{II}} = 0$, where μ_0 and ε_0 are the permeability and permittivity of vacuum, respectively:

$$\begin{aligned}\frac{\partial \chi_{y,mn}}{\partial z} &= \frac{k_{y,n}}{k_0}\sum_p \sum_q \left(\frac{k_{x,p}\gamma_{y,pq} - k_{y,q}\gamma_{x,pq}}{\varepsilon^{\mathrm{ord}}_{z,m-p,n-q}}\right) + k_0\gamma_{x,mn}\\ \frac{\partial \chi_{x,mn}}{\partial z} &= \frac{k_{x,m}}{k_0}\sum_p \sum_q \frac{\left(k_{x,p}\gamma_{y,pq} - k_{y,q}\gamma_{x,pq}\right)}{\varepsilon^{\mathrm{ord}}_{z,m-p,n-p}} - k_0\gamma_{y,mn}\\ \frac{\partial \gamma_{y,mn}}{\partial z} &= \frac{k_{y,n}}{k_0}\left(k_{x,m}\chi_{y,mn} - k_{y,n}\chi_{x,mn}\right) - \sum_p \sum_q \frac{k_0\chi_{x,pq}}{\varepsilon^{\mathrm{inv}}_{x,m-p,n-q}}\\ \frac{\partial \gamma_{x,mn}}{\partial z} &= \frac{k_{x,m}}{k_0}\left(k_{x,m}\chi_{y,mn} - k_{y,n}\chi_{x,mn}\right) - \sum_p \sum_q \frac{k_0\chi_{y,pq}}{\varepsilon^{\mathrm{inv}}_{y,m-p,n-q}}\end{aligned} \tag{6}$$

where p and q are two integers. The superscripts ord and inv indicate the coefficients of the Fourier series for $\bar{\bar{\varepsilon}}$ and its inverse, respectively, and the expressions are similar to Chen and Tan (2010). The inverse of the dielectric function is used for the sake of fast convergence of the algorithm according to the Fourier factorization rule (Li 1996). Note that different dielectric function components are used in Eq. 6 because of the anisotropy of the material. When all three components of the dielectric tensor are equal, Eq. 6 degenerates to the isotropic scenario presented in Chen and Tan (2010).

The substrate (Region III) in general can be a biaxial medium. A transmitted plane wave (forward propagating wave) in this region with an in-plane wave vector ($k_{x,m}$, $k_{y,n}$) can have two different $k^t_{z,mn}$. If the electric field is $\mathbf{E}^t_{mn} = \left(E^t_{x,mn}, E^t_{y,mn}, E^t_{z,mn}\right)$, then based on Maxwell's equation (Yeh 1979), one obtains

$$\begin{pmatrix} \varepsilon_{\mathrm{III},x}k_0^2 - k_{y,n}^2 - \left(k^t_{z,mn}\right)^2 & k_{x,m}k_{y,n} & k_{x,m}k^t_{z,mn} \\ k_{x,m}k_{y,n} & \varepsilon_{\mathrm{III},y}k_0^2 - k_{x,m}^2 - \left(k^t_{z,mn}\right)^2 & k_{y,n}k^t_{z,mn} \\ k_{x,m}k^t_{z,mn} & k_{y,n}k^t_{z,mn} & \varepsilon_{\mathrm{III},z}k_0^2 - k_{x,m}^2 - k_{y,n}^2 \end{pmatrix} \begin{pmatrix} E^t_{x,mn} \\ E^t_{y,mn} \\ E^t_{z,mn} \end{pmatrix} = 0 \tag{7}$$

To have nontrivial plane-wave solutions, the determination of the matrix has to be zero and four solutions can be obtained. Two solutions of $k^t_{z,mn}$ that correspond to the two forward propagating waves (Li 1998) are used to express the electric field in Region III as

$$\mathbf{E}_{\mathrm{III}} = \sum_{m} \sum_{n} \sum_{\sigma=1,2} E^{t}_{\sigma,mn} \mathbf{p}_{\sigma,mn} \exp\left(ik_{x,m}x + ik_{y,n}y + ik^{t}_{\sigma,z,mn}z\right) \tag{8}$$

in which

$$\mathbf{p}_{\sigma,mn} = N_{\sigma,mn} \begin{pmatrix} \left(\varepsilon_{\mathrm{III},y}k_0^2 - k_{x,m}^2 - \left(k^{t}_{\sigma,z,mn}\right)^2\right)\left(k_0^2\varepsilon_{\mathrm{III},z} - k_{x,m}^2 - k_{y,n}^2\right) - k_{y,n}^2\left(k^{t}_{\sigma,z,mn}\right)^2 \\ k_{x,m}k_{y,n}\left(k^{t}_{\sigma,z,mn}\right)^2 - k_{x,m}k_{y,n}\left(\varepsilon_{\mathrm{III},z}k_0^2 - k_{x,m}^2 - k_{y,n}^2\right) \\ k_{x,m}k_{y,n}^2 k^{t}_{\sigma,z,mn} - k_{x,m}k^{t}_{\sigma,z,mn}\left(\varepsilon_{\mathrm{III},y}k_0^2 - k_{x,m}^2 - \left(k^{t}_{\sigma,z,mn}\right)^2\right) \end{pmatrix} \tag{9}$$

is the polarization vector for the electric field with diffraction order (m, n) and σ is the index for the two forward propagating waves. Note that $N_{\sigma,mn}$ is a coefficient that normalizes $\mathbf{P}_{\sigma,mn}$.

The magnetic field for Regions I and III can be obtained from the electric field based on Maxwell's equation. The complex coefficients in the field expressions are then solved through matrix manipulations by matching the tangential component of the electric and magnetic field between adjacent layers. Once the coefficients are solved, the spectral directional-hemispherical reflectance (R)`, spectral directional-hemispherical transmittance (T), as well as the field distributions in each layer can be obtained. Note that if the substance is isotropic like the structure to be discussed in this work, the field expression in Eq. 8 will be the same as isotropic RCWA (Chen and Tan 2010). In this case, the only difference between the isotropic and anisotropic RCWA exists in Eq. 6.

The spectral directional absorptance of a structure can be obtained from $\alpha = 1 - R - T$ based on energy balance, and the spectral directional emissivity ε is equal to the absorptance based on Kirchhoff's law. For opaque structures, $T = 0$ and thus $\varepsilon = \alpha = 1 - R$. To illustrate the local absorption profile inside the structure, the local power dissipation density in W/m^3 can be calculated based on (Zhao and Zhang 2015b)

$$w(x,y,z) = \frac{1}{2}\mathrm{Re}\left\{-i\omega\varepsilon_0\bar{\bar{\varepsilon}}\mathbf{E}\cdot\mathbf{E}^*\right\} = \frac{1}{2}\varepsilon_0\omega\left(\varepsilon_x''|E_x|^2 + \varepsilon_y''|E_y|^2 + \varepsilon_z''|E_z|^2\right) \tag{10}$$

in which $\mathbf{E}$ is the complex electric field obtained from RCWA. The absorptance of a certain volume or layer can be calculated by the ratio of the absorption inside the volume over the incident power (Zhao et al. 2014, 2015):

$$\alpha = \frac{\iiint \omega(x,y,z)dV}{0.5c_0\varepsilon_0|\mathbf{E}_{\mathrm{inc}}|^2 A\cos\theta} \tag{11}$$

The denominator is the incident power on area A at a polar angle θ. Using Eq. 11, the absorptance inside a certain volume can be retrieved. The integration over the whole structure yields the same absorptance with 1-R-T.

2.3 Surface Plasmon Polaritons and Magnetic Polaritons in Nanostructures

Generally speaking, the reason of the unique optical and radiative properties of the nano-/microstructures is the excitation of various polaritons, which are also of critical importance in near-field radiative heat transfer between two objects, as discussed in ▶ Near Field Radiative Transfer. Polaritons are quasiparticles resulting from strong coupling of electromagnetic waves with an electric or magnetic dipole-carrying excitation. One of such excitations is plasmons, which are quasiparticles associated with oscillations of plasma, i.e., a collection of charged particles inside the materials. The external electromagnetic wave can couple with a surface plasmon (SP), which is a collective oscillation of surface charges, to form a surface plasmon polariton (SPP) (Barnes et al. 2003; Zayats et al. 2005). SPPs have been intensively studied for applications in lithography (Srituravanich et al. 2004), chemical and bio-sensing (Homola 2008), extraordinary optical transmission (Barnes et al. 2003), and optical communication (Ozbay 2006). Upon the excitation of SPPs, the charges close to the surface are driven by the electric field and oscillate back and forth intensively. The field of an SPP is confined near the surface with the amplitude exponentially decaying away from the interface. Not only is a surface wave induced propagating along the interface with an amplitude exponentially decaying away from the interface (Raether 1988; Ghaemi et al. 1998; Barnes et al. 2003; Zayats et al. 2005; Marquier et al. 2007; Chen and Chen 2013), but the oscillation of charges also dissipates the electromagnetic energy into heat, creating strong absorption at the resonance frequency.

SPPs are non-radiative surface waves since the required wave vector is larger than the free space wave vector, and they do not couple with propagating electromagnetic waves in vacuum (Zhang 2007). This can be seen from the magnitude of the wave vector of the SPs on a metal-dielectric interface that can be expressed as (Zhang 2007)

$$|\mathbf{k}_{\mathrm{SP}}| = k_0 \sqrt{\frac{\varepsilon_1 \varepsilon_2}{\varepsilon_1 + \varepsilon_2}} \tag{12}$$

where $k_0 = \omega/c_0$ is the magnitude of the wave vector in vacuum, and ε_1 and ε_2 here are the dielectric functions of the dielectric and metal, respectively. Note that Eq. 12 is for nonmagnetic materials and transverse magnetic (TM) waves. For transverse electric (TE) waves, the excitation of SPs requires a magnetic material with negative permeability. The wave vector of the electromagnetic waves must have a tangential component equal to $\mathbf{k}_{\mathrm{SP}}$ to excite SPPs. Since $|\mathbf{k}_{\mathrm{SP}}|$ is greater than k_0, high index prisms can be used to increase the wave vector of the incident waves so that SPs can

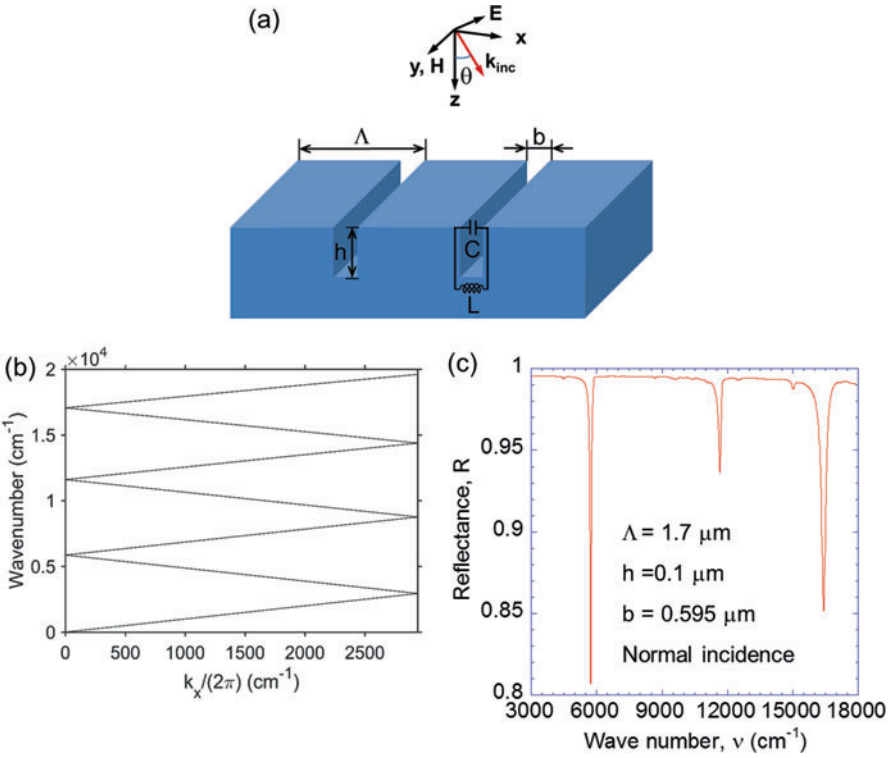

Fig. 3 (**a**) Schematic of the 1D grating with a period Λ, height or depth h, ridge width w, and trench width b. The equivalent LC circuit model is also shown with the capacitance C and inductance L. The wave vector $\mathbf{k_{inc}}$ of the incident plane wave is in the x-z plane at an angle θ with respect to the z-axis. (**b**) Folded dispersion of SPPs for a Ag grating with $\Lambda = 1.7$ μm, $h = 0.1$ μm, and $b = 0.595$ μm. (**c**) Normal reflectance of TM waves for a Ag grating with the same geometries with (**b**)

couple with incident light to excite SPPs. Another method is taking advantage of the diffracted light by periodic micro-/nanostructures, as will be explained in the following.

Consider a 1D silver (Ag) grating on a semi-infinite Ag substrate shown in Fig. 3 (a). The grating has a periodicity in the x-direction described by $\Lambda = 1.7$ μm. The grating height is $h = 0.1$ μm and the trench width is $b = 0.595$ μm. The incident wave is a plane wave with an oscillating magnetic field in the y-direction (i.e., TM wave). For this 1D grating, the Bloch-Floquet condition presented in Eq. 2 becomes $k_{x,m} = k_{x,\text{inc}} + 2\pi m/\Lambda$. Thus, the dispersion relation can be folded into the region for $k_x \leq \pi/\Lambda$, and SPPs can be excited on a grating surface with propagating waves in air. Figure 3b shows the folded dispersion relation of SPPs for the given Ag grating. Unless mentioned specifically, the optical properties of Ag in this work are obtained using a Drude model (Zhang 2007; Modest 2013). The intersections of the folded dispersion with the vertical axis identify the location where SPPs can be

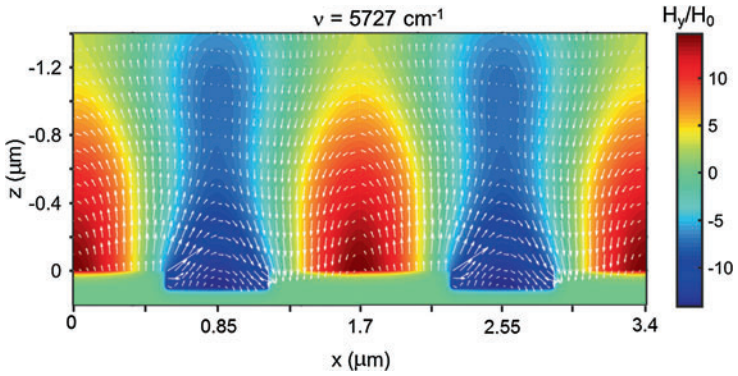

Fig. 4 Instantaneous field distribution at the excitation of SPP at $\nu = 5727\ \text{cm}^{-1}$ for an Ag grating with $\Lambda = 1.7$ μm, $h = 0.1$ μm, and $b = 0.595$ μm. The incident wave is at normal direction and TM-polarized. Color represents the relative magnetic field and the arrows show the electric field

excited for a normal incidence, as shown in Fig. 3c. Note that the plane of incidence is set as the *x*-*z* plane for normal incidence. Since the grating is 1D and the electric field of TM waves is in the *x*-direction, $\theta = \psi = \phi = 0^{\circ}$ and $k_y = 0$. The excitation of surface polaritons is responsible for the dips in the reflectance, whose frequency locations agree well with predictions of the dispersion curves. Figure 4 illustrates an instantaneous field distribution at $\nu = 5{,}727\ \text{cm}^{-1}$ corresponding to the first reflectance dip in Fig. 3c. The colors represent direction and magnitude of the magnetic field and the arrows show the electric field. Note that this surface wave is a standing wave since the incident photon can couple with two surface plasmons at normal incidence: one corresponds to $m = +1$ with a wave vector $k_{\text{sp}} = 2\pi/\Lambda$ (right traveling) and the other corresponds to $m = -1$ with $k_{\text{sp}} = -2\pi/\Lambda$ (left traveling). The two surface waves form a standing wave with a wavelength that is nearly equal to the period of the grating. At oblique incidence, only one SPP can be excited and thus the surface wave is not a standing wave (Zhao et al. 2015).

Note that ε_1 and ε_2 in Eq. 12 need to have different signs. For typical metal, since ε_2 has a negative real part whose magnitude is much larger than ε_1, the dispersion of SPP is very close to the light line, which is $k_0 = \omega/c_0$. On the other hand, in some cases where ε_2 has a positive real part, another type of surface waves that has a similar dispersion called Wood's anomaly (WA) (Nguyen-Huu et al. 2012) may be supported. Wood's anomaly occurs when a diffraction order shows up at the grazing angle, and its dispersion can be expressed as $|\mathbf{k}_{\|,mn}| = k_0$, which is essentially the light line (Lee et al. 2008a). Both SPP and WA can be used to tailor the optical and radiative properties, as will be discussed later.

Another type of polaritons that has been widely studied is magnetic polariton (MP). MPs refer to the strong coupling of the magnetic resonance inside a micro-/nanostructure with the external electromagnetic waves (Wang and Zhang 2009, 2012a, b; Mattiucci et al. 2012; Pardo et al. 2011; Lee et al. 2008b; Wang et al. 2014). This type of resonance was initially discovered and experimentally

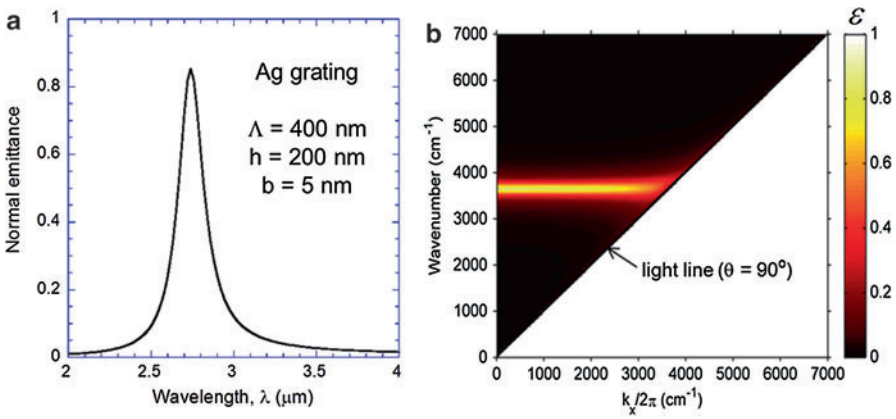

Fig. 5 Emittance for Ag deep gratings with $\Lambda = 400$ nm, $h = 200$ nm, and $b = 5$ nm: (**a**) Normal spectral emittance; (**b**) contour plot of the emittance in terms of the wavenumber and parallel component of the wave vector. The vertical line with $k_x = 0$ represents normal direction and the diagonal represents grazing angle or *light line* (From Zhao and Zhang 2014)

demonstrated in split-ring resonator (Linden et al. 2004), metal-rod pairs (Podolskiy et al. 2002), and fishnet structures (Zhang et al. 2005) that are possessed of negative permeability in the microwave region. The radiative properties of MPs have also been experimentally studied as have been summarized in a recent review (Zhang and Wang 2013). Take the grating in Fig. 3a as an example, if the geometries change to $\Lambda = 400$ nm, $h = 200$ nm, and $b = 5$ nm, for TM waves, this deep grating can support MP that is characterized by an emittance peak as high as 0.85 at the wavelength of 2.74 μm in the normal emittance spectrum shown in Fig. 5a. The emittance enhancement is remarkable since the emittance is less than 0.005 for a smooth Ag surface at this wavelength. Compared to SPPs, MPs show less angle dependence as shown in Fig. 5b.

The excitation of this MP is caused by the oscillating magnetic field of the incident waves. Under the time-varying magnetic field parallel to the *y*-direction, an oscillating current is produced around the grooves in the *x*-*z* plane, generating a strong magnetic field according to Faraday's law. Figures 6a, b show the instantaneous electromagnetic and current-density field when the MP occurs in the Ag grating. The magnetic field, represented by the color contour, is the square of the relative amplitude. Since the instantaneous electric and current-density field vectors oscillate with time, the direction of the arrows may reverse. The big arrows show the general direction of the vectors. The current-density vectors are obtained from $\mathbf{J} = \sigma\mathbf{E}$ where σ is the complex electrical conductivity of the material at the given location (Zhang 2007), and they form a closed loop around the trench. The strongest magnetic enhancement corresponding to the closed current loop is at the bottom of the trench, where the magnitude of magnetic field is more than 30 times that of the incident waves, showing a strong diamagnetic effect. Meanwhile, when the

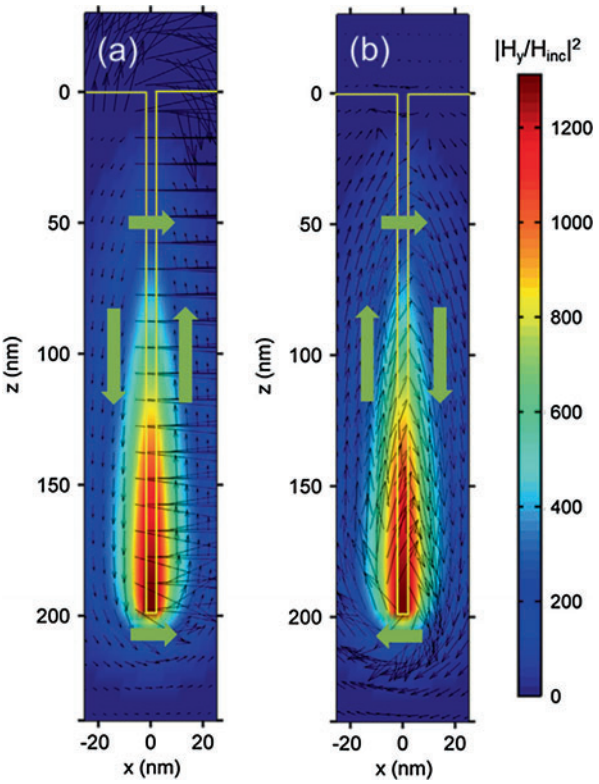

Fig. 6 (**a**) The electromagnetic field and (**b**) current-density distribution in the Ag grating with the same parameters as for Fig. 5 at $\lambda = 2.74$ μm. The color contour shows the relative magnitude of the y component of the magnetic field. The vectors show the direction and magnitude of the electric field in (**a**) and current density in (**b**) (From Zhao and Zhang 2014)

resonance happens, charges tend to accumulate at the upper corner of the grating, and this in turn creates a strong electric field around the trench opening.

Based on the closed current loop, an equivalent LC circuit model (Wang and Zhang 2009, 2011, 2012b; Engheta 2007; Solymar and Shamonina 2009; Zhao and Zhang 2014) shown in Fig. 3a can be used to predict the magnetic resonance condition. The air in the trenches serves as a dielectric capacitor and the surrounding metallic material acts as an inductor. Since the walls on both sides of the groove are close to each other, mutual inductance L_m needs to be considered. It can be evaluated from the parallel-plate inductance formula and written as $L_m = \mu_0 hb/l$, where μ_0 is the permeability of vacuum and l is the length in the y-direction that can be set to unity for 1D gratings. The other contribution of the inductance comes from the kinetic energy of charges since charge current must accelerate to create the currents (Solymar and Shamonina 2009). Thus, kinetic inductance L_k is introduced and added to the mutual inductance to form the total inductance in the circuit. It can be obtained from the frequency-dependent complex impedance of the metal, $Z_k \equiv R_k - i\omega L_k$, where ω is the angular frequency. The impedance can be expressed as $Z_k = s/(\sigma A_{eff})$, where s is the total length of the current path in the metal and A_{eff} is the effective cross-sectional area of the induced electric current. For the deep grating structure,

$s = 2h + b$ and $A_{\text{eff}} = \delta l$, where $\delta = \lambda/2\pi\kappa$ is the penetration depth of electric field, in which κ is the extinction coefficient, $\sigma = -i\omega\varepsilon\varepsilon_0$ is the electrical conductivity. After some manipulations, the following expression can be obtained:

$$L_{\text{k}} = -\frac{2h+b}{\varepsilon_0\omega^2 l\delta}\frac{\varepsilon'}{\left(\varepsilon'^2+\varepsilon''^2\right)} \tag{13}$$

The capacitance of the vacuum inside the trench can be approximated by

$$C = c'\varepsilon_0\frac{hl}{b} \tag{14}$$

where c' is a numerical factor between 0 and 1 accounting for the nonuniform charge distribution between the ridges of the grating (Wang and Zhang 2011; Zhou et al. 2006). Without using a full-wave simulation, c' can be taken as an adjustable parameter that is about 0.5. Since resistance elements do not affect the resonance frequency, only the imaginary part of the total impedance of the LC circuit is considered and can be expressed by

$$Z_{\text{tot}} = i\omega\left(L_{\text{k}} + L_{\text{m}} - \frac{1}{\omega^2 C}\right) \tag{15}$$

By setting $Z_{\text{tot}} = 0$, one obtains the magnetic resonance wavelength as

$$\lambda_{\text{R}} = 2\pi c_0\sqrt{(L_{\text{k}} + L_{\text{m}})C} \tag{16}$$

where c_0 is the speed of light in vacuum, which is an implicit equation because L_{k} is frequency- or wavelength-dependent. Note that l does not show up in this equation and can be assumed unity in later discussions. If $c' = 0.5$ is used in Eq. 16, the LC model yields a resonance at $\lambda_{\text{R}} = 2.78$ μm, which agrees well with the RCWA simulation (Zhao and Zhang 2014). For other structures like slit array and metal/dielectric/metal structures (Wang and Zhang 2009, 2012b), the inductance and capacitance in the circuits can be obtained in a similar way.

2.4 Polarization Dependence of Radiative Properties

The shape of the periodic patterns in metamaterials can induce polarization dependence. For metamaterial absorbers designed for energy harvesting purpose, patterns with polarization-independent radiative properties may be preferred (Wang and Wang 2013). However, some shapes can induce polarization-dependent response and can be used to design metamaterials with polarization control ability. These structures have recently attracted a lot of attention for their potential applications in multiband and dual-band absorption (Sakurai et al. 2015), nonlinear optics, holography, chemical sensing, and anomalous refraction (Grady et al. 2013;

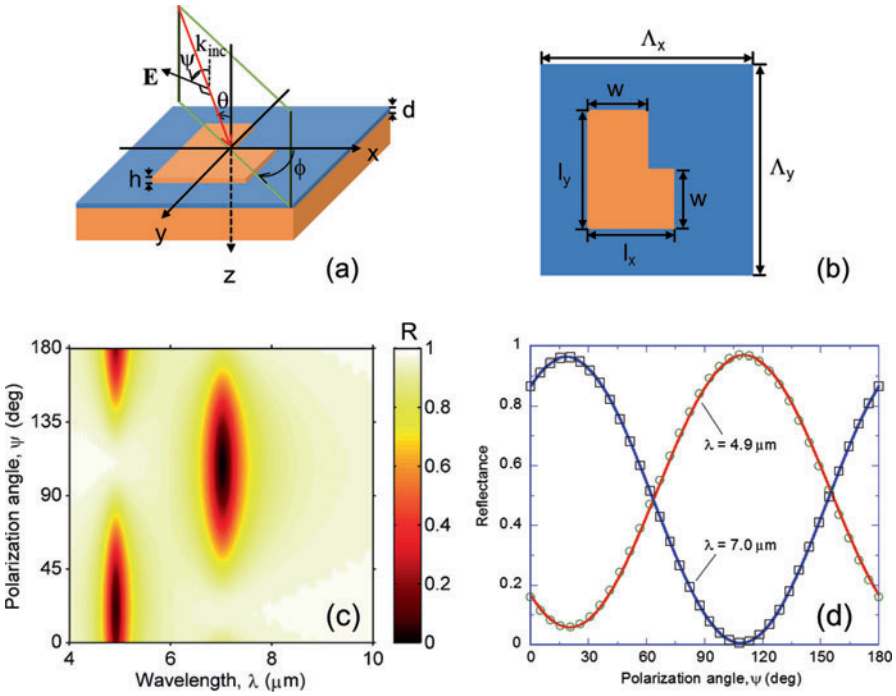

Fig. 7 (**a**) Illustration of the L-shape metal/dielectric/metal structure, the plane of incidence, incident wave vector, electric field vector, polar angle θ, azimuthal angle ϕ, and polarization angle ψ. (**b**) The x-y plane view of the structure. (**c**) Normal reflectance contours obtained from FDTD simulations. (**d**) Simulated normal reflectance as a function of the polarization angle at $\lambda = 4.9$ μm and 7.0 μm (Reproduced reflectance from the simulated reflectance for $\psi = 0°$, $\psi = 90°$, and $\psi = 45°$ using the three-polarization-angle method are shown with markers. From Zhao et al. 2016)

Cui et al. 2014). Here, the focus is the anisotropic radiative properties of metamaterial structures.

Consider a 2D anisotropic metal/dielectric/metal structure shown in Fig. 7a, b. The middle layer is an Al_2O_3 layer with a thickness $d = 140$ nm, sandwiched between the L-shape patterned 100-nm-thick (h) gold layer and a gold ground plane that is opaque. The top metallic pattern is at the center of the unit cell and repeats periodically with the same period $\Lambda_x = \Lambda_y = 3.2$ μm. The width $w = 0.85$ μm and the L-shape pattern have two arms with different lengths: $l_x = 1.275$ μm and $l_y = 1.7$ μm. The commercial Lumerical FDTD software is used to compute the radiative properties. At normal incidence, the reflectance shows highly polarization dependence as demonstrated in Fig. 7c, especially at the two resonances due to MPs at the wavelengths $\lambda = 4.9$ and 7.0 μm (Sakurai et al. 2015). Only at a certain polarization angle (i.e., the polarization of the eigenmodes) can the MPs be fully excited and cause minimum reflectance. It may be easy to identify this polarization angle for the symmetric structures. However,

if the arms of the L shape are not equal, the dependence on polarization angle becomes more complicated, and three-polarization-angle method can be used.

For a plane wave with arbitrary polarization incident from a vacuum to a medium, the reflectance is (Zhao et al. 2016)

$$\begin{aligned} R_\psi &= \left|r_{ss}\ \sin\psi + r_{ps}\ \cos\psi\right|^2 + \left|r_{sp}\ \sin\psi + r_{pp}\ \cos\psi\right|^2 \\ &= R_{\mathrm{TE}}\ \sin^2\psi + R_{\mathrm{TM}}\ \cos^2\psi + R_{\mathrm{C}}\ \sin(2\psi) \end{aligned} \tag{17}$$

Here, r_{ss} and r_{pp} are the co-polarized reflection coefficients and r_{sp} and r_{ps} are the cross-polarized reflection coefficients. The first and second subscripts describe the polarization status of the reflected and incident waves, respectively. For isotropic medium, no cross polarization can occur; thus, $r_{sp} = r_{ps} = 0$. $R_{\mathrm{TE}} = |r_{sp}|^2 + |r_{ss}|^2$ and $R_{\mathrm{TM}} = |r_{pp}|^2 + |r_{ps}|^2$ are the reflectance for TE and TM waves, respectively, and $R_{\mathrm{C}} = \mathrm{Re}\left(r_{ss}r_{ps}^*\right) + \mathrm{Re}\left(r_{pp}r_{sp}^*\right)$, which is generally nonzero but can be either positive or negative due to cross polarization. This means reflectance as a function of polarization angle can be determined once three unknowns are solved using three reflectance for different ψ. Eq. 17 can be recast as

$$R_\psi = A\ \sin(2\psi + \chi) + \overline{R} \tag{18}$$

where $A = \sqrt{(R_{\mathrm{TM}} - R_{\mathrm{TE}})^2/4 + R_{\mathrm{C}}{}^2}$ is the amplitude and $\overline{R} = (R_{\mathrm{TE}} + R_{\mathrm{TM}})/2$ is the average reflectance for TE and TM waves. The phase $\chi \in (-\pi, \pi]$ is determined by $\sin\chi = (R_{\mathrm{TM}} - R_{\mathrm{TE}})/2A$ and $\cos\chi = R_{\mathrm{C}}/A$. Based on Eq. 18, the reflection maximum and minimum, which correspond to the two eigenmodes, occur at $\psi_1 = \pi/4 - \chi/2$ and $\psi_2 = \psi_1 + \pi/2$, respectively. Figure 7d shows the reflectance with markers as a function of polarization angle reproduced using the reflectance for TE, TM, and $\psi = 45°$. As the plot shows, the reproduced results agree with the full-wave simulation. $\psi_1 = 18.6°$ and $\psi_2 = 108.6°$ can thus be determined. Though the matrix method for anisotropic medium (Schubert 1996; Yariv and Yeh 2002) may be applied to find the polarizations for the eigenmodes, the three-polarization-angle method may be more convenient since the reflectance and transmittance can be identified directly.

3 Applications of Periodic Nano-/Microstructures and Metamaterials

Periodic nano-/microstructures and metamaterials have attractive characteristics for many applications such as bio- and chemical sensing, Raman spectroscopy, solar photovoltaics and TPVs, thermoelectric energy conversion, hot electron solar cells and photodetectors, and water splitting and undercooled boiling (Boriskina et al. 2013). This chapter discusses a specific application in TPV systems. Wavelength-

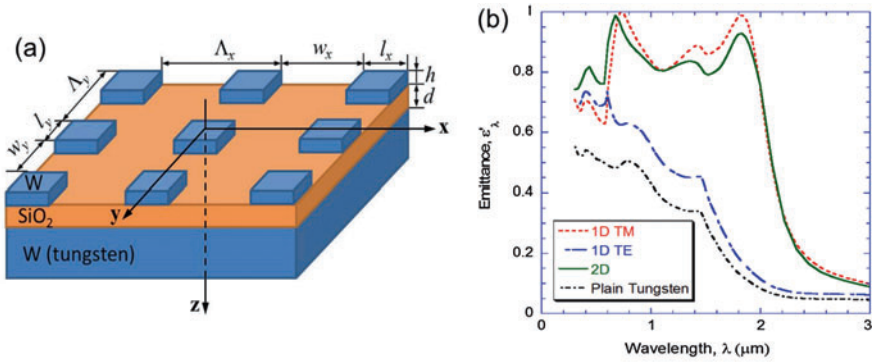

Fig. 8 (**a**) Illustration of the numerical model for the 2D metal/dielectric/metal nanostructure. The parameters are $\Lambda_x = \Lambda_y = 600$ nm, $l_x = l_y = 300$ nm, and $h = d = 60$ nm. (**b**) Normal emittance spectra of the 2D structure and a 1D structure for both TE and TM waves, along with that of plain tungsten (From Zhao et al. 2013)

selective emitters are of critical importance to improving the efficiency of TPV systems and solar TPV systems (Basu et al. 2007; Zhou et al. 2016; Bierman et al. 2016; Khodasevych et al. 2015). An ideal TPV emitter should not only be wavelength-selective, but also desired to be polarization-insensitive so that high emittance for both TE and TM waves can be achieved (Nguyen-Huu et al. 2012). Micro-/nanostructures of wide profile diversity can tailor thermal radiation by utilizing different physical mechanisms. Not only 1D gratings (Nguyen-Huu et al. 2012; Chen and Zhang 2007), V-groove gratings (Sergeant et al. 2010), and photonic crystals (Nagpal et al. 2008; Narayanaswamy and Chen 2004; Lee et al. 2007) but also various 2D nano-/microstructures (Heinzel et al. 2000; Pralle et al. 2002; Sai and Yugami 2004; Sai et al. 2003, 2005; Chen and Tan 2010; Song et al. 2016; Zhao and Fu 2016) and multilayer structures (Bouchon et al. 2012; Wang et al. 2007; Cui et al. 2011; Hendrickson et al. 2012; Lévêque and Martin 2006; ; Liu et al. 2010, 2011b; Puscasu and Schaich 2008; Wang et al. 2012; Deng et al. 2015) have been investigated for their wavelength-selective properties. Here, a typical 2D metal/dielectric/metal periodic nanostructure is discussed for TPV applications (Zhao et al. 2013).

Figure 8a is a schematic of the considered structure. The grating is made of rectangular tungsten (W) patches whose lateral dimensions are l_x and l_y with a height h and periods Λ_x and Λ_y. The periodic arrays of patches are on a thin dielectric film SiO_2 of thickness d that is deposited on a tungsten substrate. Tungsten is chosen as the emitter material because it is corrosion resistant and can withstand high temperatures. In the present study, the geometric parameters are fixed as follows: $\Lambda_x = \Lambda_y = 600$ nm, $l_x = l_y = 300$ nm, and $h = d = 60$ nm. Figure 8b compares the normal emittance spectra for the 2D structure and a 1D counterpart of the proposed structure from Wang and Zhang (2012b) for both TE and TM waves. The emittance spectrum for plain tungsten is also shown. The spectrum for the 1D structure with

TM waves and that for the 2D structures are very similar; both contain two major emission peaks (near 0.7 and 1.8 μm) that do not exist in the spectra for the TE wave or plain tungsten. The overall emittance at normal direction is the average of those for TE and TM waves. As an example, at $\lambda = 1.7$ μm, the normal overall emittance for the 2D structure is 0.85 and only 0.58 for the 1D structure. Therefore, the throughput and efficiency of the TPV system can be significantly improved with the 2D structure. The structure is designed for a TPV cell that has a bandgap at around 2 μm, such as $In_{0.2}Ga_{0.8}Sb$. For cells with a different bandgap, the emittance spectrum can be optimized by tuning the geometries of the structure.

The emittance peaks at $\lambda = 1.83$ μm and 0.7 μm are critical for the shape of the spectrum. The emittance peak around $\lambda = 0.7$ μm is because of Wood's anomaly. It can be seen from Fig. 8b that only TM waves can cause a high Wood's anomaly emittance peak for 1D gratings, but can be accomplished for both TE and TM waves for 2D gratings. Note that this peak is not due to SPP since the dielectric function of tungsten has a positive real part between 0.24 and 0.92 μm (Palik 1985). At longer wavelengths, however, the real part can go negative and SPPs can be excited. Figure 9a illustrates the contour plot of the emittance for the 2D structure at TM waves in terms of wavenumber and the x-component of the free-space wave vector. The bright oblique bands indicate the emittance enhancement due to SPPs or Wood's anomaly, while the flat bright band around 5,400 cm^{-1} is due to the excitation of MP as will be discussed later. The effect of the periodicity in the x- direction can be analyzed by considering $n = 0$. In this case, surface waves (can be SPPs or Wood's anomaly) can exist once the following dispersion relation is satisfied:

$$k_{sw} = \left| k_{inc} \sin\theta + \frac{2\pi m}{\Lambda_x} \right| \tag{19}$$

This dispersion relation is solved with different m values (-2, -1, 0, and $+1$) for surface waves excited between air and tungsten, and solutions of this equation for SPPs are marked as circles in Fig. 9a for demonstration purpose and the same for the following contour plots. Since SPPs are quite close the light line, the solutions are essentially the dispersion for Wood's anomaly. These circles follow the bright emittance band well obtained from the 2D RCWA calculation. The periodicity in the y-direction (Λ_y) can affect the dispersion of the surface waves as well. Take $m = 0$ and $n \neq 0$ for simplicity. The incident wave will be diffracted into the y-direction, and the dispersion relation becomes

$$k_{sw} = \sqrt{(k_{inc} \sin\theta)^2 + \left(\frac{2\pi n}{\Lambda_y}\right)^2} \tag{20}$$

The solutions of this equation for SPPs are marked on Fig. 9a with triangles and they agree well. Within the considered ranges of frequency and wave vector, only the surface waves associated with $n = \pm 1$ show up when $m = 0$. This branch will fold with the grating period Λ_x in the x-direction and show up as $m = \pm 1, \pm 2$ orders.

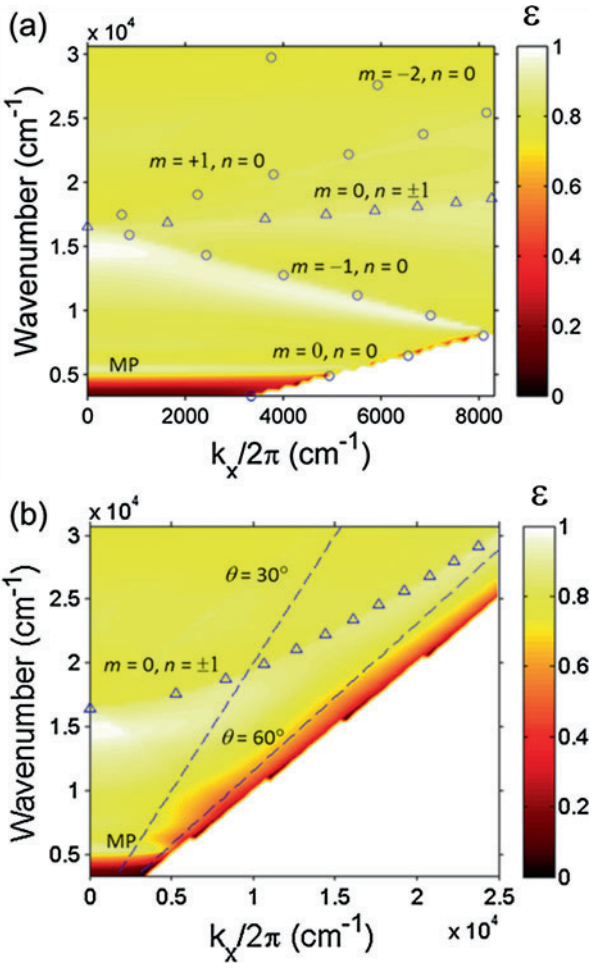

Fig. 9 Emittance contour plots of the 2D grating/thin-film structure from RCWA calculations along with the SPP dispersion relations: (**a**) TM waves; (**b**) TE waves (From Zhao et al. 2013)

However, these higher orders also do not show up in the contour plot due to the intrinsic losses of tungsten.

For TE incident waves, the periodicity in the y-direction plays a crucial role to excite surface waves and create a high emittance peak. Figure 9b shows the emittance contour for TE waves. For TE wave incidence with $\phi = 0°$, the order n must not be zero since k_y must have a nonzero real part. A bright resonance band can be observed whose resonance frequency increases with k_x. This branch is identified as the surface wave with $m = 0$ and $n = \pm 1$ and can be matched by the predictions from Eq. 20 as shown by the triangles.

The emittance peak at $\lambda = 1.83$ μm is due to MP. When the MP is excited, the magnetic field is strongly enhanced in the dielectric layer inserted between the tungsten grating and tungsten substrate, as shown in Fig. 10. The instantaneous

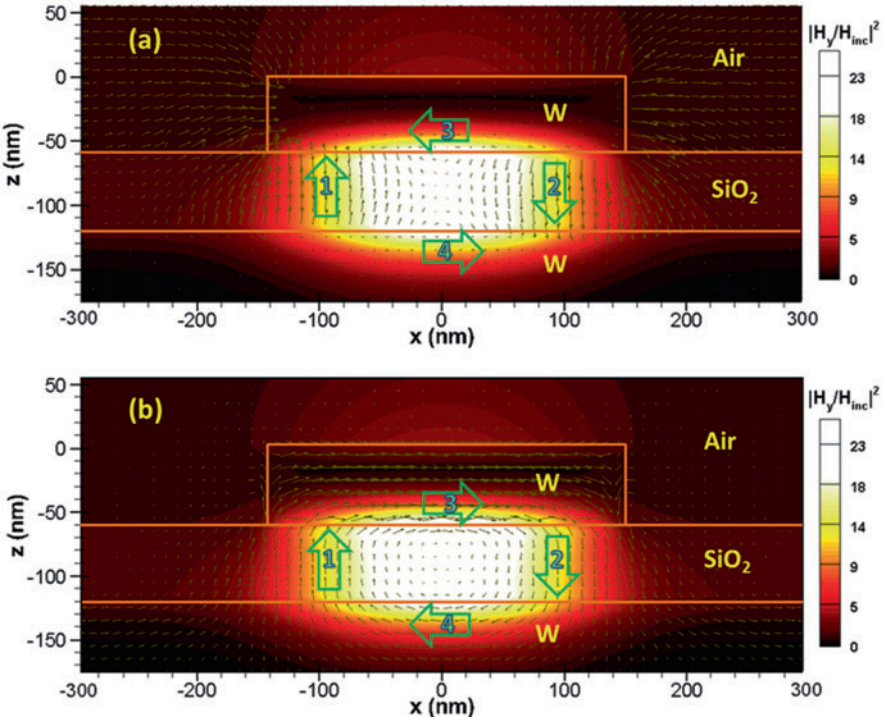

Fig. 10 The electromagnetic fields and current density distribution in the 2D structure for TM waves at normal incidence and $\lambda = 1.83$ μm. The fields are calculated at $y = 0$ in the x-z plane. The *color* shows the relative magnitude of the y component of the magnetic field. The vectors show the direction and magnitude of (**a**) the electric field and (**b**) current density (From Zhao et al. 2013)

electric field and current density vectors are denoted by the arrows, while the magnetic field is represented by the color contour. The current density vector $\mathbf{J} = \sigma\mathbf{E}$ can be expressed as the sum of the conduction current and displacement current: $\mathrm{Re}(\mathbf{J}) = \mathbf{J}_{\mathrm{cond}} + \mathbf{J}_{\mathrm{disp}} = \sigma' \mathrm{Re}(\mathbf{E}) - \sigma'' \mathrm{Im}(\mathbf{E})$. For locations 1 and 2 (marked on Fig. 10), the displacement current is the dominant contribution and has the same direction as the electric field. For locations 3 and 4, the conduction and displacement current densities have opposite signs, but the magnitude of the displacement current density is more than twice greater than the conduction current density, make the full current density follow the direction of the displacement current density. Therefore, the displacement is of critical importance for the formation of the current loop. Since the instantaneous electric field vectors in Fig. 10 will oscillate with time, the direction of the arrows may reverse but should always be antiparallel.

4 Tailoring Thermal Radiation Using 2D Materials

Emerging 2D materials offer another exciting new element to construct metamaterials with unique thermal radiative properties (Grigorenko et al. 2012). Not only can 2D materials be patented to different shapes like ribbons and resonators to control optical and radiative properties, but they also can be used as an element to construct hybrid structures with other micro-/nanostructures to create exotic properties. Using a hybrid structure with a monolayer graphene covered on a metal grating, Zhao et al. (2014, 2015) and Zhao and Zhang (2015a) demonstrated strong absorption through excitation of SPPs and MPs. Fan's group (Piper and Fan 2014; Zhu et al. 2016) utilized critical coupling in graphene/photonic crystal hybrid structures to achieve perfect absorption. Plasmonic optical nanoantennas with different shapes can also be hybridized with 2D materials to capture light efficiently (Echtermeyer et al. 2011; Yao et al. 2014). The hybrid structures may open a novel route to engineer radiative properties by enabling plentiful coupling effects between graphene plasmonic resonances with SPPs and MPs in traditional plasmonic metamaterials. This section reviews the recent work on optical and radiative properties of 2D materials and hybrid structures. Graphene and hBN will be discussed specifically.

4.1 Optical and Radiative Properties of Graphene and Its Ribbons

With a layer of carbon atoms arranged in a honeycomb lattice, graphene exhibits unique electronic, thermal, mechanical, and optical properties (Nair et al. 2008; Thongrattanasiri et al. 2012; Pop et al. 2012). Since its discovery in 2004 (Novoselov et al. 2004), graphene has been extensively studied for potential applications in nanoelectronics, optoelectronics, plasmonics, transformation optics, and energy conversion (Vakil and Engheta 2011; Xia et al. 2009; Liu et al. 2011a; Yao et al. 2013; Echtermeyer et al. 2011; Miao et al. 2012; Messina and Ben-Abdallah 2013; Wu et al. 2009). Unlike in conventional solids where electrons are described by the Schrödinger equation, electrons in graphene are governed by the Dirac equation for 2D relativistic fermions (Mics et al. 2015). This enables a saturation absorption in the visible and near-infrared region and actively tunable surface plasmons in mid- and far-infrared region (Grigorenko et al. 2012; Nair et al. 2008) with relatively low loss compared to traditional plasmonic materials that have a lot of potential applications in electro-optics, optical communications, and energy conversion (Basov et al. 2014; Li et al. 2008; Fang et al. 2013a; Vakil and Engheta 2011; Xia et al. 2009; Liu et al. 2011a; Yao et al. 2013; Echtermeyer et al. 2011; Miao et al. 2012; Messina and Ben-Abdallah 2013; Wu et al. 2009).

The radiative properties of graphene can be described by its sheet conductivity σ_s, which consists of the contribution from intraband (Drude-like term) and interband transitions, i.e., $\sigma_s = \sigma_D + \sigma_I$, respectively (Falkovsky 2008):

$$\sigma_D = \frac{i}{\omega + i/\tau}\frac{2e^2 k_B T}{\pi\hbar^2}\ln\left[2\cosh\left(\frac{\mu}{2k_B T}\right)\right] \tag{21}$$

and

$$\sigma_I = \frac{e^2}{4\hbar}\left[G\left(\frac{\hbar\omega}{2}\right) + i\frac{4\hbar\omega}{\pi}\int_0^\infty \frac{G(\xi) - G(\hbar\omega/2)}{(\hbar\omega)^2 - 4\xi^2}d\xi\right] \tag{22}$$

where $G(\xi) = \sinh(\xi/k_B T)/[\cosh(\mu/k_B T) + \cosh(\xi/k_B T)]$. Here, e is the electron charge, $\hbar$ is the reduced Planck constant, and k_B is the Boltzmann constant. Otherwise specified, the following parameters are used in all the calculations presented in this work: chemical potential $\mu = 0.3$, relaxation time $\tau = 10^{-13}$ s, and temperature $T = 300$ K. Since μ can be tuned by electrical gating or chemical doping, the optical properties of graphene can be actively tuned (Novoselov et al. 2004). Figure 11 illustrates the effect of μ. As the plot shows, in the visible and near infrared, interband transitions dominate and graphene shows a wavelength-independent conductivity $\sigma_s = \sigma_0 = e^2/(4\hbar)$, making graphene to have no plasmonic response but have wavelength-independent absorptivity of about 2.3% (Nair et al. 2008). In the mid- and far- infrared region, graphene can support highly confined SPs. For a graphene sheet surrounded by media with dielectric functions ε_1 and ε_2 on each side of graphene, respectively, the dispersion of the graphene surface plasmon satisfies

$$\frac{\varepsilon_1}{\sqrt{k_{GSP}^2 - \varepsilon_1 k_0^2}} + \frac{\varepsilon_2}{\sqrt{k_{GSP}^2 - \varepsilon_2 k_0^2}} = -\frac{i\sigma_s}{\omega\varepsilon_0} \tag{23}$$

where k_{GSP} is the wave vector for the plasmon and ε_0 is the permittivity of vacuum. Figure 12a shows a schematic of graphene SPs.

In the mid- and far-infrared region, the intraband transitions dominate, and the conductivity can be approximately expressed in a Drude-like model $\sigma_s = e^2\mu\tau/(\pi\hbar^2 - i\pi\omega\tau\hbar^2)$ (García de Abajo 2014). In this wavelength region, if graphene is surrounded by vacuum, i.e., $\varepsilon_1 = \varepsilon_2 = 1$, the dispersion can be simplified as (Vakil and Engheta 2011)

$$k_{GSP} = \frac{\omega}{c_0}\sqrt{\varepsilon_1 - \frac{4\varepsilon_0}{\sigma_s^2\mu_0}} \approx \frac{2i\omega\varepsilon_0}{\sigma_s} \tag{24}$$

where μ_0 is the vacuum permeability.

Graphene resonators such as ribbons (Brar et al. 2013; Nikitin et al. 2012; Strait et al. 2013; Yan et al. 2013; Liu et al. 2014), disks (Yi et al. 2015; Koppens et al. 2011; Yan et al. 2012; Fang et al. 2013b) and cross shapes (Fallahi and Perruisseau-Carrier 2012) have been studied for their coherent radiative properties. The plasmons in ribbons, for example, cannot propagate freely since they are reflected on the

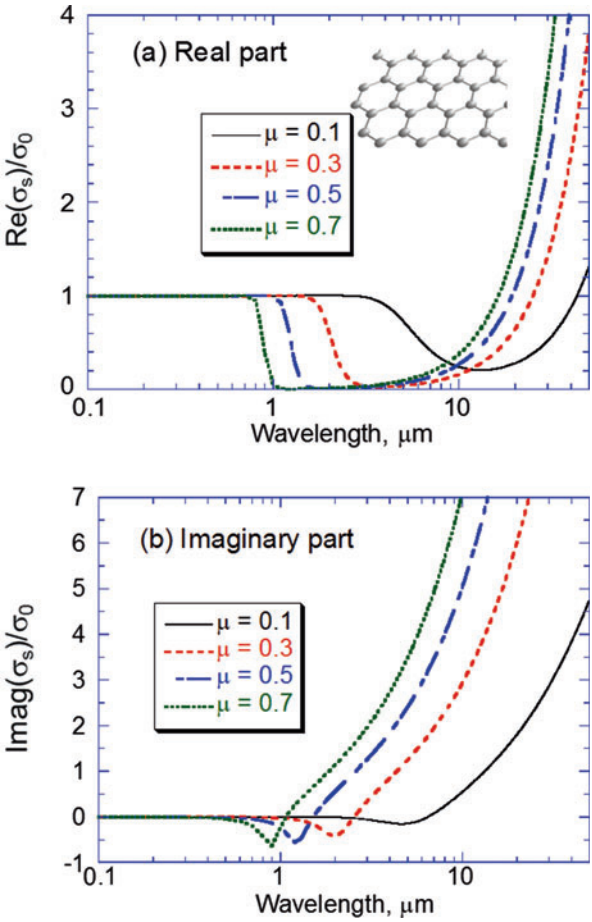

Fig. 11 Real and imaginary part of the sheet conductivity of graphene with different chemical potentials: (**a**) real part and (**b**) imaginary part

ribbon edges with a phase shift $\Delta\varphi$ (Chen et al. 2013; Garcia-Pomar et al. 2013). The resonance can be described by a Fabry-Pérot model:

$$\Delta\varphi + \mathrm{Re}(k_{\mathrm{GSP}})r = m\pi \tag{25}$$

where integer m denotes the resonance order, r is the width of the ribbon, and Re takes the real part of the complex quantity. By substituting Eq. 24, the resonance condition of suspended ribbons in vacuum can be expressed as (Du et al. 2014)

$$\omega = \sqrt{\frac{e^2\mu(m - \Delta\varphi/\pi)}{2\varepsilon_0\hbar^2 r}} \tag{26}$$

At normal incidence, plasmons initiated from the two edges of the ribbon are out of phase, and thus only the plasmons associated with odd m's can show up. The

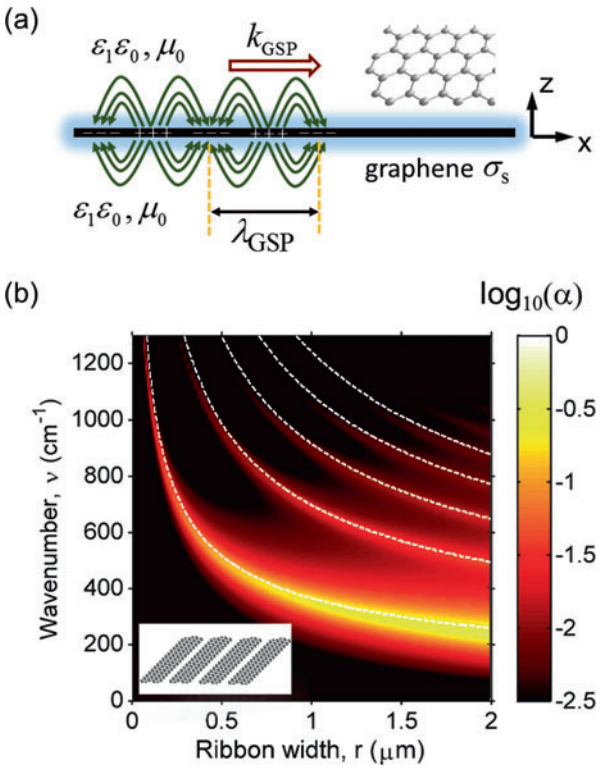

Fig. 12 (**a**) Schematic of graphene surface plasmon (GSP). (**b**) The normal absorptance contour of a free-standing graphene ribbon array with $\Lambda = 4$ μm and $\mu = 0.3$ eV, where the *dashed lines* are the predictions of Eq. 26 with $\Delta\varphi = \pi/4$ (From Zhao and Zhang 2015a)

plasmons with even m's can occur at oblique incidence since in-phase plasmons can be excited from the two edges (Du et al. 2014). It is recently found that $\Delta\varphi$ is $\pi/4$ for free-standing ribbons in vacuum (Nikitin et al. 2014; Du et al. 2014). Figure 12(b) shows the absorptance (α) contour of a suspended graphene ribbon arrays at normal incidence obtained with RCWA. The dashed lines, from bottom to top, are the predictions from Eq. 26 with $m = 1$, 3, 5, and 7, respectively. The frequency of the resonance is inversely proportional to $\sqrt{r}$. Note that the highest absorptance occurs for $m = 1$ at $r \approx 2$ μm with a value near 0.35. For the other branches with higher orders, the absorption by graphene ribbons is even smaller.

4.2 Graphene-Covered Metal Gratings

As shown in Fig. 12b, though graphene can be patterned into different periodic resonators to boost the absorptance, high absorptance or emittance is difficult to achieve solely with graphene resonators due to its atomically thin thickness. One way to solve this problem is to combine 2D materials together with nano-/microstructures. Here, a hybrid structure consists of graphene and grating is considered, as shown in Fig. 13a. The Ag grating geometries are $\Lambda = 400$ nm, $b = 30$ nm,

and $h = 200$ nm. A monolayer graphene is covered on top of the grating. Figure 13b compares the absorptance spectra for the plain grating and graphene-covered grating. For TM waves at $\theta = 10°$, there exist three distinct peaks at $\nu = 6{,}700\ \text{cm}^{-1}$ (1.49 μm), $18{,}350\ \text{cm}^{-1}$ (545 nm), and $20{,}930\ \text{cm}^{-1}$ (478 nm), which are associated, respectively, with the excitation of the fundamental MP (MP1), the second-order MP (MP2), and an SPP. Clearly, the graphene increases the peak absorptance significantly without shifting the peak locations. This is because of the unique properties of graphene at visible and near-infrared region. The effect of the graphene across the trench opening can be considered by modifying the LC circuit for grating, as shown in Fig. 13a. The additional impedance introduced by the graphene layer, $Z_G = b/\sigma_s$, is a real number since σ_s is dominated by the interband contribution σ_I at the resonance wavelengths. This makes the graphene layer behave like a pure resistor across the trench. Since the impedance of graphene is real and very large, the resonance wavelength of MP is not affected. However, the graphene layer does add resistance to the circuit, making the resonance peaks broader (lower Q factor).

The absorption enhancement is achieved by coupling MP resonance with the graphene. As Fig. 6 shows, at the excitation of MP, a strong electric field is created at the trench opening. Thus, graphene acts like a pure resistor surrounded by a strongly enhanced local electric field and thus dissipates significant power. The power dissipation profile at MP1 resonance for the plain and covered grating is depicted in Fig. 14. It is clear that the absorption in the Ag walls delineating the trench is not enhanced, but somewhat weakened by the added graphene layer. However, the local absorption in the graphene sheet across the opening of the trench is extremely strong with a maximum w on the order of 10^8W/m^3, which is three orders of magnitude higher than the highest w in the grating region. In fact, one can use Eq. 11 to evaluate the absorptance in graphene, which is as high as 0.68 and nearly 30 times higher than the absorptance of a free-standing graphene sheet. Similar mechanism and phenomena hold for the MP2 and SPP resonance peaks, and the absorptance in graphene can be even higher at the SPP excitation (Zhao et al. 2014, 2015). Since graphene has a remarkably high carrier mobility up to $200{,}000\ \text{cm}^2\ \text{V}^{-1}\ \text{s}^{-1}$ at room temperature for both electrons and holes (Novoselov et al. 2004), this enhanced absorption in graphene has potential applications in ultrafast optoelectronic devices such as transistors (Engel et al. 2012) and photodetectors (Xia et al. 2009; Mueller et al. 2010; Furchi et al. 2012; Fang et al. 2012).

However, in the mid- and far-infrared region, graphene has plasmonic behavior, and the plasmonic resonance inside the graphene can strongly couple with the MP resonances inside metal gratings to form a new hybrid plasmonic system and create tunable coherent radiative properties. Consider a graphene ribbon-grating hybrid structure illustrated in Fig. 15a. The grating geometries are $\Lambda = 4$ μm, $b = 300$ nm, and $h = 2$ μm. The ribbon edges are touched with the Ag grating. For TM waves, the absorptance spectra of the plain and ribbon-covered structure are shown in Fig. 15b. For the plain grating, the MP resonance is at $1{,}041\ \text{cm}^{-1}$ with an absorptance of 0.35. After covering ribbons on the grating, the absorptance is boosted to 0.94, and the resonance shifts to $1{,}086\ \text{cm}^{-1}$, indicating a strong coupling between graphene and the grating that is quite different with previous case in the visible and near-

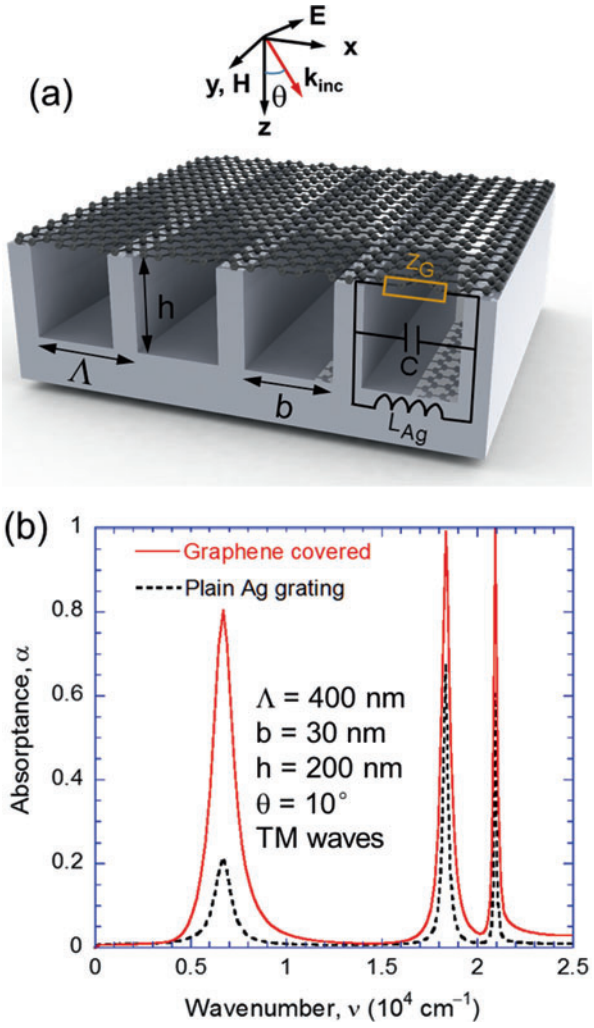

Fig. 13 (**a**) Schematic of the graphene-covered 1D grating nanostructure for a plane TM wave incident at an angle of θ. The inset shows the corresponding LC circuit model for the hybrid structure. (**b**) Comparison of the absorptance of the graphene-covered and plain Ag grating with $h = 200$ nm, $\Lambda = 400$ nm, and $b = 30$ nm at incidence angle $\theta = 10^{\circ}$ for TM waves (From Zhao et al. 2015)

infrared region. The spectrum of the free-standing ribbon array without the grating is also given for comparison. In this case, the ribbon plasmon gives rise to a small absorption peak around 650 cm^{-1}. The resonances with and without graphene can be successfully modeled using the equivalent LC circuit shown in Fig. 13a. The graphene in this case serves as an inductor across the trench that lowers the total inductance in the circuit and shifts MP resonance to a higher frequency.

To better explain the coupling effect, Fig. 16 compares the absorptance contours at normal incidence for four different configurations versus the trench width. The plain gratings support MP resonances as shown in Fig. 16a. The frequency of the MP increases with b and reaches an asymptotic value when $b > 0.25$ μm because of the effect of kinetic inductance as has been explained previously. The dot markers are

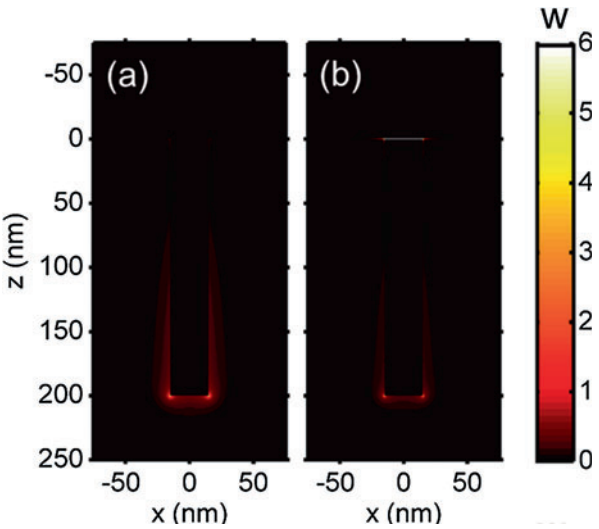

Fig. 14 Power dissipation profiles for the two structures when $\theta = 10^\circ$ at MP1 resonance ($\nu = 6700\ \mathrm{cm}^{-1}$): (**a**) The plain Ag grating and (**b**) the graphene-covered grating. The unit of w is $10^5\ \mathrm{W/m^3}$ and the scale bar limit is $6 \times 10^5 \mathrm{W/m^3}$, beyond which w is shown in *white* color (From Zhao et al. 2015)

the predictions of the LC model. The absorptance contour stays the same if the graphene ribbon is covered only on the ridges of the grating, as shown in Fig. 16b. The graphene ribbons appear to have no effect on the resonance since they are in contact with the metal on one side. On the contrary, if the ribbons are suspended above the trench openings, as the case in the inset of Fig. 16c, the plasmonic resonances of the ribbons show up and the absorptance becomes more plentiful. The bright bands that exhibit a dependence on $1/\sqrt{b}$ are caused by the plasmons in ribbons. Note that the edges of the ribbons are always in touch with Ag. Although the shape of these bands is similar to the free-standing ribbon array resonances, the resonances in Fig. 16c cannot be predicted with Eq. 26 using the reflection phase shift $\pi/4$. In fact, since the edge is touched with Ag instead of vacuum, the tangential component of the electric field (E_z) at the edges needs to vanish at the boundary due to the high conductivity of Ag, resulting in a phase shift of $-\pi$ for the plasmon waves. This can be further justified by the excellent agreement between the simulation and the prediction results of Eq. 26 with $\Delta\varphi = -\pi$, which are shown as diamond markers. Note that the plasmons are all associated with odd m's since the incidence is normal. Covering the grating by a continuous graphene, as illustrated in Fig. 16d, yields the same absorptance contour as Fig. 16c. Again, the portion of the graphene on the ridges has little contribution on the resonance. Thus, in terms of the radiative properties, covering a continuous graphene is equivalent to suspending a periodic ribbon array over the grating trenches. Since the fabrication of the structure with continuous graphene on grating can be realized with the existing fabrication technique (Papasimakis et al. 2010), it provides a realistic way to experimentally achieve the coupling between MP and plasmons in ribbon array.

The chemical potential of graphene can be used to actively modify the coupling picture by changing the dispersion of the graphene plasmons. For example, Fig. 17 shows the absorptance spectra for the structure shown in Fig. 15a with various μ. The

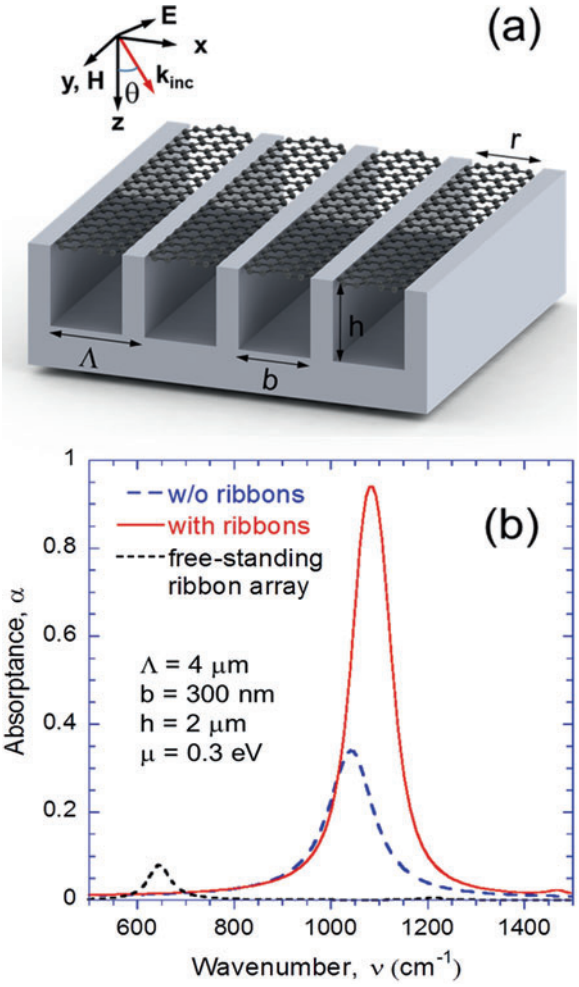

Fig. 15 (**a**) Schematic of the hybrid grating-graphene ribbon plasmonic structure. (**b**) The absorptance spectrum for the plain Ag grating, free-standing ribbon array, and ribbon-covered grating ($r = b$). The geometries for the grating are given in the figure (From Zhao and Zhang 2015a)

case when $\mu = 0.3$ eV corresponds to the solid spectrum in Fig. 15b. If μ changes to 0.28 eV or 0.32 eV, the ribbon plasmon shifts to a slightly lower or higher frequency, respectively, and the coupling strength decreases as the peak absorptance becomes lower. When μ is further decreases to $\mu = 0.2$ eV, two bumps at 871 cm^{-1} and 1,164 cm^{-1} occur that are due to the plasmons associated with $m = 1$ and 3, respectively. However, neither of them can couple with the MP, whose absorptance drops down to about 0.4. Similarly, at $\mu = 0.5$ eV, the plasmon in ribbons associated with $m = 1$ moves to 1,412 cm^{-1} and totally decouples with the MP. Therefore, the chemical potential can be tuned to control plasmons in the ribbons to couple or decouple with the MP resonance in the grating. Besides the chemical potentials, geometry parameters like the ribbon width and the elevation can also be used to tune the radiative properties of the structure (Zhao and Zhang 2015a).

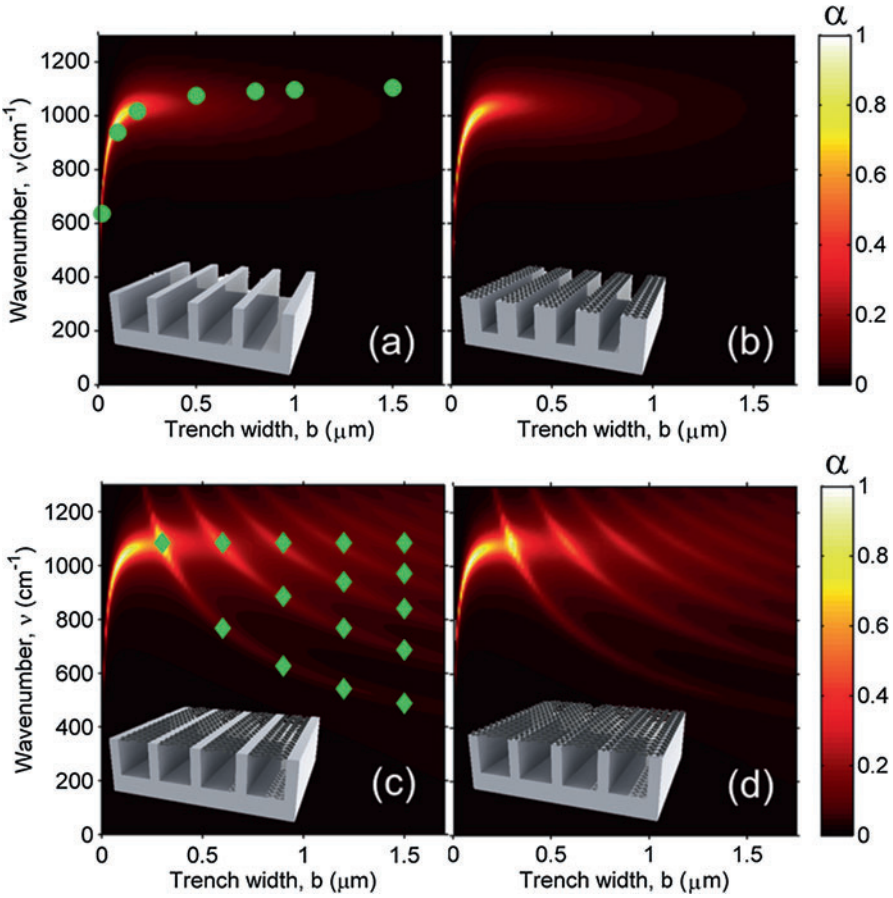

Fig. 16 Absorptance contours for four different structures when $\Lambda = 4$ μm, $h = 2$ μm, and $\mu = 0.3$ eV are fixed and b changes: (**a**) plain Ag grating; (**b**) graphene ribbons covering the Ag grating ridges; (**c**) graphene ribbons covering the trench opening ($r = b$); and (**d**) continuous graphene sheet covering the whole grating. The *round markers* are the predictions of Eq. 16 and the *diamond markers* are the predictions of Eq. 26 with $\Delta\varphi = -\pi$ (From Zhao and Zhang 2015a)

4.3 Hexagonal Boron Nitride-Covered Metal Gratings

As a material that has a similar lattice structure with graphene, hexagonal boron nitride (hBN) has been used as an ideal substrate supporting high-quality graphene (Dean et al. 2010; Yan et al. 2016). While 2D plasmonic materials and semiconductors have been studied extensively because of their potential applications in microelectronic, optoelectronic, and photonic devices (Li et al. 2016), few studies have yet explored the potentials of using phononic 2D materials to achieve perfect absorption through coupling with nano-/microstructures, especially for materials like hBN that is a hyperbolic material. Considering that hBN can survive at 1,500 °C in air

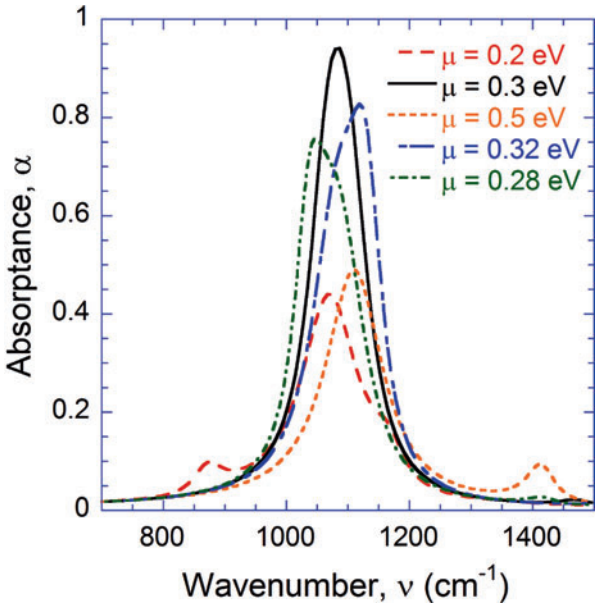

Fig. 17 The absorptance spectra of the structure shown in Fig. 15 with different graphene chemical potentials (From Zhao and Zhang 2015a)

(Liu et al. 2013), accomplishing strong absorption or emission bands in the infrared region with hBN films holds great significance for high-temperature energy harvesting applications (Khodasevych et al. 2015).

Hyperbolic materials refer to uniaxial materials whose axial and tangential permittivities have opposite signs. The isofrequency surfaces obey a hyperbolic shape instead of a closed sphere for common isotropic materials. Subsequently, these materials can support propagating modes with very large tangential wave vectors and thus can have unique applications in sub-wavelength imaging (Caldwell et al. 2014; Dai et al. 2015a; Li et al. 2015) and heat transfer (Jacob et al. 2012; Nefedov et al. 2013; Biehs et al. 2012; Poddubny et al. 2013). The hyperbolic response of hBN is mainly caused by its optical phonon vibrations. The real part of the dielectric function of hBN is shown in Fig. 18a. The two mid-infrared Reststrahlen bands due to the optical phonon modes are evident. The in-plane phonon modes ($\omega_{\mathrm{TO},\perp} = 1{,}370\ \mathrm{cm}^{-1}$ and $\omega_{\mathrm{LO},\perp} = 1{,}610\ \mathrm{cm}^{-1}$) and out-of-plane phonon modes ($\omega_{\mathrm{TO},\parallel} = 780\ \mathrm{cm}^{-1}$ and $\omega_{\mathrm{TO},\parallel} = 830\ \mathrm{cm}^{-1}$) contribute to the in-plane (**E** lies in the *x*-*y* plane, denoted by $\perp$) and out-of-plane (**E** parallel to the optical axis or the *z*-direction, denoted by $\parallel$) dielectric functions, respectively (Kumar et al. 2015):

$$\varepsilon_{\xi} = \varepsilon_{\infty,\xi}\left(1 + \frac{\omega_{\mathrm{LO},\xi}^2 - \omega_{\mathrm{TO},\xi}^2}{\omega_{\mathrm{TO},\xi}^2 - i\gamma_{\xi}\omega - \omega^2}\right) \tag{27}$$

where $\xi = \parallel, \perp$. The other parameters used are $\varepsilon_{\infty,\parallel} = 2.95$, $\gamma_{\parallel} = 4\ \mathrm{cm}^{-1}$, $\varepsilon_{\infty,\perp} = 4.87$, and $\gamma_{\perp} = 5\ \mathrm{cm}^{-1}$. Since the damping coefficients γ are rather

small, the dielectric function becomes negative between the TO and LO phonon modes, making the in-plane and out-of-plane dielectric functions of hBN possess opposite signs in either Reststrahlen band. In the lower Reststrahlen band, $\varepsilon'_{||} = \varepsilon'_z < 0$ and $\varepsilon'_\perp = \varepsilon'_x = \varepsilon'_y > 0$, hBN has type I hyperbolicity, while in the upper Reststrahlen band, $\varepsilon'_x = \varepsilon'_y < 0$ and $\varepsilon'_z > 0$, hBN holds type II hyperbolicity (Jacob 2014). Meanwhile, in the two regions with hyperbolicity, loss is negligibly small.

The hyperbolic regions allow propagating waves with unbounded wave vectors as can be seen from the isofrequency surface for a uniaxial medium with the optical axis in the z-direction (Poddubny et al. 2013):

$$\frac{k_x^2 + k_y^2}{\varepsilon_{||}} + \frac{k_z^2}{\varepsilon_\perp} = \frac{\omega^2}{c_0^2} \tag{28}$$

where $\mathbf{k} = (k_x, k_y, k_z)$ represents the allowed wave vector. If loss is neglected, in the frequency ranges, the hBN possesses hyperbolicity, Eq. 28 becomes a hyperboloid, and both k_x and k_z can theoretically be infinitely large. Note that Eq. 28 is for extraordinary waves or TM waves, which are the primary interest here. For TE waves, the isofrequency surface becomes a sphere described by $|\mathbf{k}|^2 = \varepsilon_\perp \omega^2 / c_0^2$; thus, hBN behaves the same as an isotropic material with the ordinary dielectric function.

For an hBN film, hyperbolic phonon polaritons (HPPs) are supported in the two Reststrahlen bands or hyperbolic regions. Their dispersion can be obtained from the reflection coefficient of TM waves for an hBN film of a thickness d suspended in vacuum. The dispersion of HPPs can be seen by the bright bands from the contour plots of the imaginary part of reflection coefficient of a suspended hBN film in k_x-ω space (Kumar et al. 2015), shown in Fig. 18b for a 30-nm-thick hBN film in the frequency ranges near the upper hyperbolic region. For the lower upper hyperbolic region, similar dispersions exist, though not presented here. Multiple orders of HPPs exist in both hyperbolic regions, and more orders are allowed if the film thickness becomes larger. Alternatively, when $k_x >> k_0$, the dispersion can be approximately expressed as (Dai et al. 2015b)

$$k_x(\omega) = \frac{1}{d}\sqrt{-\frac{\varepsilon_{||}}{\varepsilon_\perp}}\left[p\pi \pm 2\arctan\left(\frac{1}{\sqrt{-\varepsilon_{||}\varepsilon_\perp}}\right)\right] \tag{29}$$

where p is an integer indicating the number of orders of the HPPs and the dielectric functions are for hBN. The plus and minus signs are chosen, respectively, for the upper and lower hyperbolic bands based on the shape of the dispersion curves or the direction of the group velocity (Kumar et al. 2015). The prediction from Eq. 29 is overlaid on the contour plot as dashed lines in Fig. 18b with the corresponding p. The excellent agreement suggests that Eq. 29 can provide a convenient description of HPPs and will be referred to in later discussions.

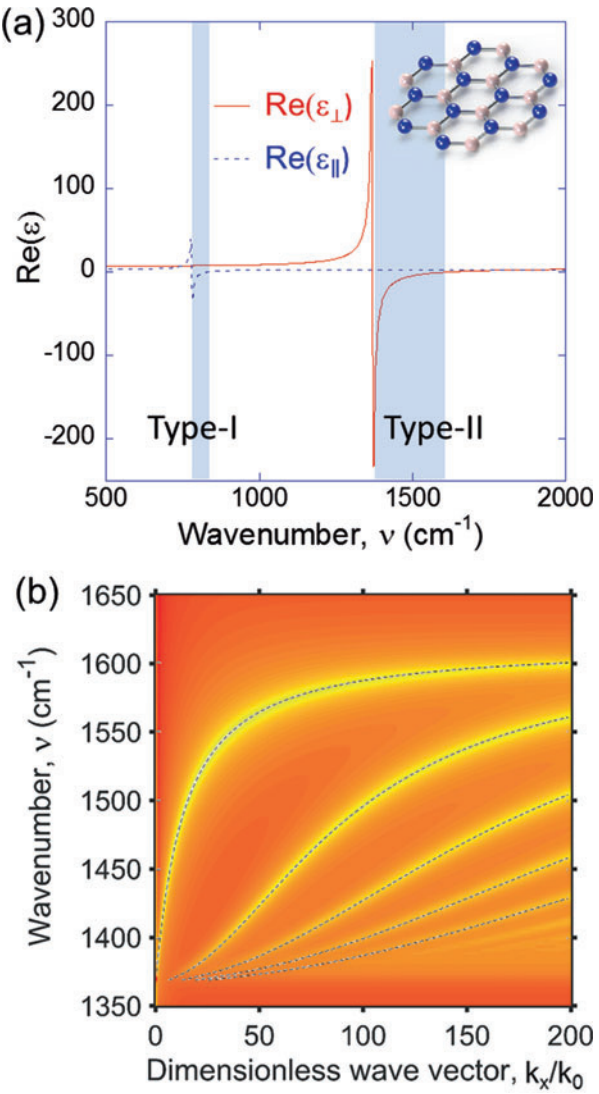

Fig. 18 (**a**) Real part of the in-plane and out-of-plane dielectric function of hBN. The two hyperbolic regions are *shaded* and marked with the corresponding type of hyperbolicity. (**b**) Contour plot showing imaginary part of reflection coefficient of TM waves for a 30-nm-thick suspended hBN film in vacuum near the upper (type II) hyperbolic region. The predictions from Eq. 29 are overlaid as *dashed curves* (From Zhao and Zhang 2017)

For both type I and type II regions, at very large $|\mathbf{k}|$, the allowed wave vectors approach the asymptotic lines described by $k_z = \pm\sqrt{-\varepsilon_\perp/\varepsilon_\parallel}k_x$ (neglecting loss) for the structure considered here since $k_y = 0$. In this case, the angle between z-axis and the Poynting vector or energy flux, the propagation angle of the polaritons, is orthogonal to the isofrequency curve that approximately equals to (Caldwell et al. 2014; Dai et al. 2015a; Li et al. 2015)

$$\beta(\omega) = \arctan\left(\sqrt{-\frac{\varepsilon_{\perp}}{\varepsilon_{||}}}\right) \tag{30}$$

Equation 30 suggests that for a given frequency, the HPPs have a unique propagation direction. As will be shown, this property plays an important role in the absorption profile of HPPs.

Figure 19a shows the geometric arrangement of the hBN/metal grating hybrid structure. Similar to previous cases, the grating is made of silver (Ag) and is periodic in the x-direction only with a period Λ, extending infinitely in the y-direction. Its trench width is b and height is h. The thickness of the covered hBN film is denoted as d. The substrate of the structure is also Ag and assumed to be semi-infinite. In reality, an Ag film whose thickness is much greater than the photon penetration depth can be deposited on another supporting substrate. Thus, the directional-spectral absorptance of the structure, α, can be calculated by $\alpha = 1-R$, where R is the directional-hemispherical reflectance of the whole structure that can be calculated using anisotropic RCWA. Figure 19b shows the normal absorptance spectra of plain gratings (dashed lines) and hBN-covered Ag gratings (solid lines) for TM waves. The geometry parameters are set as $\Lambda = 4$ μm, $b = 300$ nm, $h = 1.76$ mm, and $d = 30$ nm. One absorptance peak can be identified on the plain Ag grating spectrum, and this peak is caused by the excitation of MP resonances as explained before (Zhao and Zhang 2014). In Ag gratings, a high absorptance peak due to MP relies on an efficient coupling between the surface waves on the trench walls that can be achieved only when the trench is very narrow (Zhao and Zhang 2014). Thus, for trench width $b = 300$ nm, the absorptance peaks for plain Ag gratings are far from unit in Fig. 19b. High absorptance is difficult to achieve with thin hBN films either, as demonstrated by the absorptance spectrum of a suspended 30-nm hBN film in the plot. Only a low absorptance peak at $\omega_{\mathrm{TO},\perp}$ is obtained, since no HPPs can be excited with propagating waves in air due to the requirement of large parallel wave vectors (k_x). After covering the 30-nm hBN film on top of Ag gratings, very high absorptance can be obtained, although the frequency location is different from that of plain Ag grating. As shown in the plot, perfect absorption ($\alpha = 1$) is achieved at $\nu = 1{,}436\ \mathrm{cm}^{-1}$, which falls in the upper hyperbolic regions of hBN. This resonance is a hybrid hyperbolic phonon-plasmon polariton formed by strong coupling between plasmonic MP in the metal grating and HPPs in the hBN film.

Figure 20 shows the local power dissipation profile at the excitation of the hybrid polariton. Figure 20a is a zoomed-in picture of the hBN film, while Fig. 20b displays the dissipation profile in the structure enlarged by one order of magnitude to show the dissipation in the grating. The unit of the contour scale is $\mathrm{MW/m}^3$, while for Fig. 20b, w is multiplied by a factor of 10 to show the dissipation near the surface of the Ag groove clearly. The dissipation in the grating is similar to Fig. 14a, indicating the excitation of MP. Compared to the grating, the absorption in the hBN film becomes much stronger. In fact, the maximum w in hBN is 2.4 $\mathrm{MW/m}^3$, which exceeds the maximum value of the scale bar of 1 $\mathrm{MW/m}^3$. The whole hBN film looks bright in Fig. 20b since w is multiplied by 10. If w is integrated in the hBN film

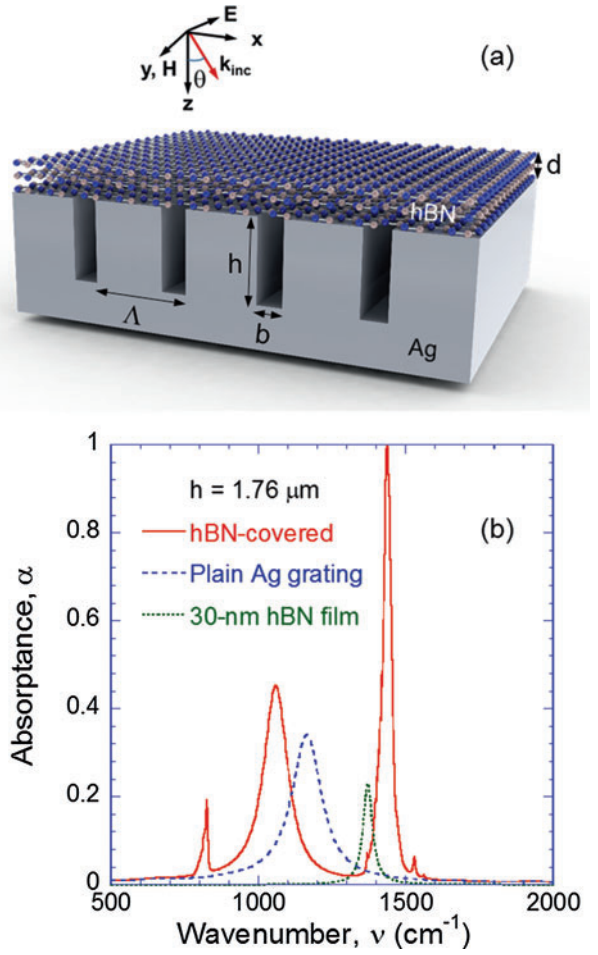

Fig. 19 (**a**) Schematic of the hBN/metal grating hybrid structure. (**b**) Absorptance spectra of plain Ag gratings (*dashed line*), hBN-covered Ag gratings (*solid line*), and a suspended 30-nm hBN film in vacuum. The geometries are $\Lambda = 4$ μm, $b = 300$ nm, $d = 30$ nm, and $h = 1.76$ μm (From Zhao and Zhang 2017)

according to Eq. 11, the absorptance of the hBN film is obtained as 0.91. Thus, most of the incoming power at the perfect and near-perfect absorption resonances is absorbed by the 30-nm hBN film instead of the grating.

Not only is the dissipation much stronger in the hBN film, but it also shows a highly location-dependent feature as shown in Fig. 20a. The white dashed lines are the surface of the grating. The dissipation density follows a zigzag path in the hBN film that is symmetric about the center of the grating, indicating that the power is nonuniformly absorbed in the film. This unique dissipation profile is caused by the HPP waveguide modes (Caldwell et al. 2014; Dai et al. 2015a; Li et al. 2015). Due to the diffraction of the grating, electric fields with large wave vectors are generated, and they excite the hyperbolic polaritons in the hBN film. The polaritons predominantly initiate from the two upper corners of the grating because of the highly concentrated electric field therein that is about 50 times of the incident waves. The

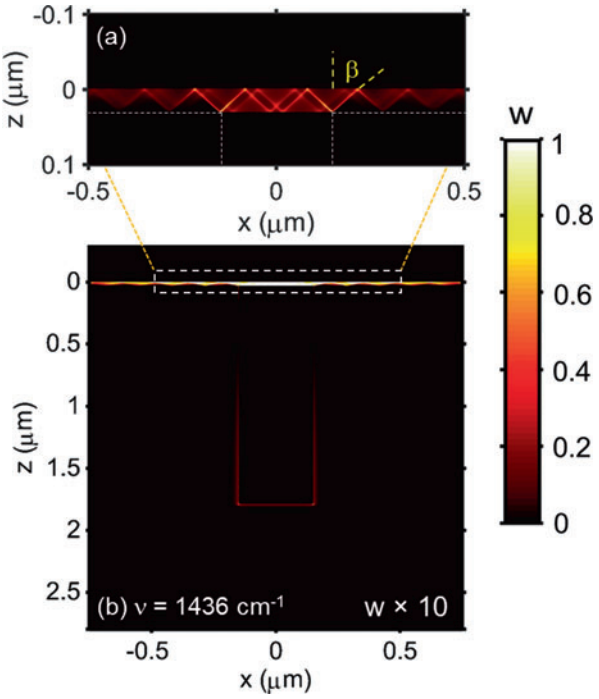

Fig. 20 Local power dissipation density profile at $\nu = 1436\ \mathrm{cm}^{-1}$ corresponding to the high-absorptance resonance in Fig. 19b: (**a**) zoomed-in profile showing the details inside the hBN film and (**b**) the dissipation profile (enlarged by one order of magnitude) of the structure. The scale bar is in $\mathrm{MW/m}^3$ with an upper limit 1 $\mathrm{MW/m}^3$, beyond which w is displayed with white color. The propagation angle β is illustrated on (**a**). Note that the x and z scales are readjusted to show the profile clearly (From Zhao and Zhang 2017)

polariton rays propagate inside the film with a fixed angle with respect to the z-axis as described in Eq. 30 and experience a total internal reflection on the top surface of the hBN film (Dai et al. 2015a). Furthermore, the period of the zigzag pattern in the x-direction can be derived as $2d \tan\beta = 2d\sqrt{-\varepsilon_\perp/\varepsilon_{||}}$. This period in real space agrees with the wave vectors of the polaritons. It should be noted that not one but multiple orders of HPPs are excited simultaneously at the resonance frequency due to grating diffraction. For a specific frequency, according to Eq. 29, the wave vectors of the multiple HPPs form an arithmetic progression with a common difference $\Delta k_x = (\pi/d)\sqrt{-\varepsilon_{||}/\varepsilon_\perp}$. Thus, these HPPs produce an interference pattern with a spatial period $2\pi/\Delta k_x$ (Dai et al. 2015a), which is the same as the above-obtained period in real space, providing a complementary way to understand the periodic zigzag pattern.

The HPPs dissipate their power as they propagate inside the film and finally vanish due to the loss of hBN. As mentioned previously, the intrinsic loss of hBN is actually very small in the hyperbolic regions, and this small loss is a critical advantage of hBN in subdiffractional focusing and imaging applications compared to hyperbolic metamaterials that are constructed with metallic nanowires or metal/dielectric multilayers (Caldwell et al. 2014; Dai et al. 2015a; Li et al. 2015). The low loss also permits long propagating length of HPPs. As Fig. 20a shows, the polaritons initiated from the grating corners experience more than five round trips before they totally disappear. Thus, the unique directional propagation of the polaritons allows

multiple reflections and long light-matter interaction distances that make strong absorption in hBN possible. In the lower hyperbolic regions, similar phenomenon can occur and has been discussed in a recent publication (Zhao and Zhang 2016). Since the propagation angle of the HPPs depends on the frequency, geometry parameters can be used to manipulate the resonance condition and the location of the absorption in hBN films. These unique properties enabled by the hybrid hBN film and grating nano-/microstructures have potential applications in sub-wavelength imaging (Li et al. 2015) and surface-enhanced Raman spectroscopy (Stiles et al. 2008). Considering that gratings made of high-temperature materials like tungsten (Zhao et al. 2013) and SiC (Wang and Zhang 2011) also support MPs, the design presented here could be used to build stable perfect absorbers or spectral-selective emitters for high-temperature applications (Khodasevych et al. 2015).

5 Conclusion and Outlook

Various numerical modeling methods are available for simulation of the optical and radiative properties of periodic nano-/microstructures. Thanks to the excitation of various polaritons such as MPs and SPPs, various micro-/nanostructures can be designed to control the optical and radiative properties for different practical application purposes. The emerging 2D materials provide even more plentiful resonances that can couple with the polaritons in the nano-/microstructures to yield exotic optical and radiative properties such as perfect absorption and tunable location-dependent absorption.

Anisotropic RCWA is summarized as a promising and competitive method to model periodic micro-/nanostructures compared to FDTD and FEM. It can simulate the radiative properties and the field distribution in the frequency domain. Because of its meshless nature, it has advantages of modeling structures with small characteristic length like 2D materials. Metal gratings can be used to excite SPPs and MPs. The wave vector of SPs can be compensated by the diffraction effect and thus help the incident electromagnetic wave to couple with the SPs to form a SPP. Localized resonance, MPs, can be excited inside the trench of the grating, and LC model can be used to model the resonance frequency. Three-polarization-angle method is discussed as a method to deduct the polarization of the eigenmodes from the reflectance or transmittance of three arbitrary polarization angles. The method may benefit the design of optical and radiative properties with polarization dependence. A 2D metal/dielectric/metal structure can be used to achieve wavelength-selective emittance that can be used to improve the efficiency of TPV system. MPs, SPPs, and WAs are responsible for the selective emittance spectrum. Different with a 1D grating, the 2D structure is insensitive to the polarization angle.

Graphene ribbons can be used to tune radiative properties. By using a graphene/metal grating hybrid structure, strong absorption can be achieved in different frequency range. In the visible and near-infrared region, graphene couples with MPs and SPPs in grating and enhances the absorptance of the structure significantly without affecting the original resonance condition of MPs and SPPs. The majority of

the power is dissipated by graphene and that can be favorable in ultrafast optoelectronic applications. In the mid- and far-infrared, graphene ribbon plasmons strongly couple with MPs in gratings to create a hybrid resonance with significantly high absorptance. The coupled resonance can be tuned by electrical gating or chemical doping of graphene. Perfect absorption is achieved in hBN/metal grating hybrid anisotropic structures due to phonon-plasmon polaritons. In the two hyperbolic regions of hBN, HPPs strongly couple with localized MPs, forming hybrid hyperbolic phonon-plasmon polaritons and achieving strong absorption. The majority of the power is dissipated inside the hBN film with a tunable location-dependent absorption profile.

Micro-/nanostructures and 2D materials provide unique platforms on which various resonances can be created, and the hybridization of them may open a novel route to engineer optical and radiative properties by enabling plentiful coupling effects. The unique optical and radiative properties can be benefitted to a lot of exciting applications over a broadband frequency range from optical to infrared, such as solar thermal technique, photodetection, chemical sensing, local heating and cooling, thermal imaging, surface-enhanced Raman spectroscopy, medical therapy, and TPVs.

Acknowledgments The research was supported by the National Science Foundation (CBET-1235975; CBET-1603761) and the US Department of Energy, Office of Science, Basic Energy Science (DE-FG02-06ER46343).

6 Cross-References

► Heat Transfer Physics: From Nano- to Macro-scales
► Introduction: Thermal Radiation Heat Transfer
► Near Field Radiative Transfer

References

Atwater HA, Polman A (2010) Plasmonics for improved photovoltaic devices. Nat Mater 9:205–213

Baida FI, Van Labeke D (2002) Light transmission by subwavelength annular aperture arrays in metallic films. Opt Commun 209:17–22

Barnes WL, Dereux A, Ebbesen TW (2003) Surface plasmon subwavelength optics. Nature 424:824–830

Basov DN, Fogler MM, Lanzara A, Wang F, Zhang Y (2014) Colloquium: graphene spectroscopy. Rev Mod Phys 86:959–994

Basu S, Chen Y-B, Zhang ZM (2007) Microscale radiation in thermophotovoltaic devices—a review. Int J Energy Res 31:689–716

Baxter J, Bian Z, Chen G, Danielson D, Dresselhaus MS, Fedorov AG, Fisher TS, Jones CW, Maginn E, Kortshagen U, Manthiram A, Nozik A, Rolison DR, Sands T, Shi L, Sholl D, Wu Y (2009) Nanoscale design to enable the revolution in renewable energy. Energy Environ Sci 2:559–588

Biehs SA, Tschikin M, Ben-Abdallah P (2012) Hyperbolic metamaterials as an analog of a blackbody in the near field. Phys Rev Lett 109:104301
Bierman DM, Lenert A, Chan WR, Bhatia B, Celanović I, Soljačić M, Wang EN (2016) Enhanced photovoltaic energy conversion using thermally based spectral shaping. Nat Energy 1:16068
Bonaccorso F, Colombo L, Yu G, Stoller M, Tozzini V, Ferrari AC, Ruoff RS, Pellegrini V (2015) Graphene, related two-dimensional crystals, and hybrid systems for energy conversion and storage. Science 347:1246501
Boriskina SV, Ghasemi H, Chen G (2013) Plasmonic materials for energy: from physics to applications. Mater Today 16:375–386
Bouchon P, Koechlin C, Pardo F, Haïdar R, Pelouard J-L (2012) Wideband omnidirectional infrared absorber with a patchwork of plasmonic nanoantennas. Opt Lett 37:1038–1040
Brar VW, Jang MS, Sherrott M, Kim S, Lopez JJ, Kim LB, Choi M, Atwater H (2014) Hybrid surface-phonon-plasmon polariton modes in graphene/monolayer h-BN heterostructures. Nano Lett 14:3876–3880
Brar VW, Jang MS, Sherrott M, Lopez JJ, Atwater HA (2013) Highly confined tunable mid-infrared plasmonics in graphene nanoresonators. Nano Lett 13:2541–2547
Bräuer R, Bryngdahl O (1993) Electromagnetic diffraction analysis of two-dimensional gratings. Opt Commun 100:1–5
Cai W, Chettiar UK, Kildishev AV, Shalaev VM (2007) Optical cloaking with metamaterials. Nat Photonics 1:224–227
Cai W, Gao T, Hong H, Sun J (2008) Applications of gold nanoparticles in cancer nanotechnology. Nanotechnol Sci Appl. doi:10.2147/NSA.S3788
Cai W, Shalaev V (2009) Optical metamaterials: fundamentals and applications. Springer, New York
Caldwell JD, Kretinin AV, Chen Y, Giannini V, Fogler MM, Francescato Y, Ellis CT, Tischler JG, Woods CR, Giles AJ, Hong M, Watanabe K, Taniguchi T, Maier SA, Novoselov KS (2014) Sub-diffractional volume-confined polaritons in the natural hyperbolic material hexagonal boron nitride. Nat Commun 5:5221
Chang C-C, Sharma YD, Kim Y-S, Bur JA, Shenoi RV, Krishna S, Huang D, Lin S-Y (2010) A surface plasmon enhanced infrared photodetector based on InAs quantum dots. Nano Lett 10:1704–1709
Chen Y-B, Chen C-J (2013) Interaction between the magnetic polariton and surface plasmon polariton. Opt Commun 297:169–175
Chen J, Nesterov ML, Nikitin AY, Thongrattanasiri S, Alonso-González P, Slipchenko TM, Speck F, Ostler M, Seyller T, Crassee I, Koppens FHL, Martin-Moreno L, García de Abajo FJ, Kuzmenko AB, Hillenbrand R (2013) Strong plasmon reflection at nanometer-size gaps in monolayer graphene on SiC. Nano Lett 13:6210–6215
Chen Y-B, Tan KH (2010) The profile optimization of periodic nano-structures for wavelength-selective thermophotovoltaic emitters. Int J Heat Mass Transf 53:5542–5551
Chen Y-B, Zhang ZM (2007) Design of tungsten complex gratings for thermophotovoltaic radiators. Opt Commun 269:411–417
Cheng F, Gao J, Luk TS, Yang X (2015) Structural color printing based on plasmonic metasurfaces of perfect light absorption. Sci Rep 5:11045
Cui Y, Fung KH, Xu J, Ma H, Jin Y, He S, Fang NX (2012) Ultrabroadband light absorption by a sawtooth anisotropic metamaterial slab. Nano Lett 12:1443–1447
Cui Y, Kang L, Lan S, Rodrigues S, Cai W (2014) Giant chiral optical response from a twisted-arc metamaterial. Nano Lett 14:1021–1025
Cui Y, Xu J, Fung KH, Jin Y, Kumar A, He S, Fang NX (2011) A thin film broadband absorber based on multi-sized nanoantennas. Appl Phys Lett 99:253101
Dahan N, Niv A, Biener G, Gorodetski Y, Kleiner V, Hasman E (2008) Extraordinary coherent thermal emission from SiC due to coupled resonant cavities. J Heat Transf 130:112401
Dai S, Fei Z, Ma Q, Rodin AS, Wagner M, McLeod AS, Liu MK, Gannett W, Regan W, Watanabe K, Taniguchi T, Thiemens M, Dominguez G, Neto AHC, Zettl A, Keilmann F,

Jarillo-Herrero P, Fogler MM, Basov DN (2014) Tunable phonon polaritons in atomically thin van der Waals crystals of boron nitride. Science 343:1125–1129
Dai S, Ma Q, Andersen T, McLeod AS, Fei Z, Liu MK, Wagner M, Watanabe K, Taniguchi T, Thiemens M, Keilmann F, Jarillo-Herrero P, Fogler MM, Basov DN (2015a) Subdiffractional focusing and guiding of polaritonic rays in a natural hyperbolic material. Nat Commun 6:6963
Dai S, Ma Q, Liu MK, Andersen T, Fei Z, Goldflam MD, Wagner M, Watanabe K, Taniguchi T, Thiemens M, Keilmann F, Janssen GCAM, Zhu SE, Jarillo Herrero P, Fogler MM, Basov DN (2015b) Graphene on hexagonal boron nitride as a tunable hyperbolic metamaterial. Nat Nanotechnol 10:682–686
Davidson DB (2010) Computational electromagnetics for RF and microwave engineering. Cambridge University Press, UK
Dean CR, Young AF, Meric I, Lee C, Wang L, Sorgenfrei S, Watanabe K, Taniguchi T, Kim P, Shepard KL, Hone J (2010) Boron nitride substrates for high-quality graphene electronics. Nat Nanotechnol 5:722–726
Deng H, Li Z, Stan L, Rosenmann D, Czaplewski D, Gao J, Yang X (2015) Broadband perfect absorber based on one ultrathin layer of refractory metal. Opt Lett 40:2592–2595
Didari A, Menguc MP (2015) Near- to far-field coherent thermal emission by surfaces coated by nanoparticles and the evaluation of effective medium theory. Opt Express 23:A547–A552
Du L, Tang D, Yuan X (2014) Edge-reflection phase directed plasmonic resonances on graphene nano-structures. Opt Express 22:22689–22698
Ebbesen TW, Lezec HJ, Ghaemi HF, Thio T, Wolff PA (1998) Extraordinary optical transmission through sub-wavelength hole arrays. Nature 391:667–669
Echtermeyer TJ, Britnell L, Jasnos PK, Lombardo A, Gorbachev RV, Grigorenko AN, Geim AK, Ferrari AC, Novoselov KS (2011) Strong plasmonic enhancement of photovoltage in graphene. Nat Commun 2:458
Engel M, Steiner M, Lombardo A, Ferrari AC, Löhneysen H, Avouris P, Krupke R (2012) Light–matter interaction in a microcavity-controlled graphene transistor. Nat Commun 3:906
Engheta N (2007) Circuits with light at nanoscales: optical nanocircuits inspired by metamaterials. Science 317:1698–1702
Falkovsky LA (2008) Optical properties of graphene. J Phys Conf Ser 129:012004
Fallahi A, Perruisseau-Carrier J (2012) Design of tunable biperiodic graphene metasurfaces. Phys Rev B 86:195408
Fan S (2014) Photovoltaics: an alternative 'Sun' for solar cells. Nat Nanotechnol 9:92–93
Fang Z, Liu Z, Wang Y, Ajayan PM, Nordlander P, Halas NJ (2012) Graphene-antenna sandwich photodetector. Nano Lett 12:3808–3813
Fang Z, Thongrattanasiri S, Schlather A, Liu Z, Ma L, Wang Y, Ajayan PM, Nordlander P, Halas NJ, García de Abajo FJ (2013a) Gated tunability and hybridization of localized plasmons in nanostructured graphene. ACS Nano 7:2388–2395
Fang Z, Wang Y, Schlather AE, Liu Z, Ajayan PM, García de Abajo FJ, Nordlander P, Zhu X, Halas NJ (2013b) Active tunable absorption enhancement with graphene nanodisk arrays. Nano Lett 14:299–304
Freitag M, Chiu H-Y, Steiner M, Perebeinos V, Avouris P (2010) Thermal infrared emission from biased graphene. Nat Nanotechnol 5:497–501
Furchi M, Urich A, Pospischil A, Lilley G, Unterrainer K, Detz H, Klang P, Andrews AM, Schrenk W, Strasser G, Mueller T (2012) Microcavity-integrated graphene photodetector. Nano Lett 12:2773–2777
García de Abajo FJ (2014) Graphene plasmonics: challenges and opportunities. ACS Photon 1:135–152
Garcia-Pomar JL, Nikitin AY, Martin-Moreno L (2013) Scattering of graphene plasmons by defects in the graphene sheet. ACS Nano 7:4988–4994
Geim AK, Grigorieva IV (2013) Van der Waals heterostructures. Nature 499:419–425
Ghaemi HF, Thio T, Grupp DE, Ebbesen TW, Lezec HJ (1998) Surface plasmons enhance optical transmission through subwavelength holes. Phys Rev B 58:6779–6782

Glytsis EN, Gaylord TK (1990) Three-dimensional (vector) rigorous coupled-wave analysis of anisotropic grating diffraction. J Opt Soc Am A 7:1399–1420
Grady NK, Heyes JE, Chowdhury DR, Zeng Y, Reiten MT, Azad AK, Taylor AJ, Dalvit DAR, Chen H-T (2013) Terahertz metamaterials for linear polarization conversion and anomalous refraction. Science 340:1304–1307
Greffet J-J, Carminati R, Joulain K, Mulet J-P, Mainguy S, Chen Y (2002) Coherent emission of light by thermal sources. Nature 416:61–64
Grigorenko AN, Polini M, Novoselov KS (2012) Graphene plasmonics. Nat Photonics 6:749–758
Heinzel A, Boerner V, Gombert A, Bläsi B, Wittwer V, Luther J (2000) Radiation filters and emitters for the NIR based on periodically structured metal surfaces. J Mod Opt 47:2399–2419
Hendrickson J, Guo J, Zhang B, Buchwald W, Soref R (2012) Wideband perfect light absorber at midwave infrared using multiplexed metal structures. Opt Lett 37:371–373
Hesketh PJ, Zemel JN, Gebhart B (1986) Organ pipe radiant modes of periodic micromachined silicon surfaces. Nature 324:549–551
Homola J (2008) Surface plasmon resonance sensors for detection of chemical and biological species. Chem Rev 108:462–493
Hou-Tong C, Antoinette JT, Nanfang Y (2016) A review of metasurfaces: physics and applications. Rep Prog Phys 79:076401
Howell JR, Menguc MP, Siegel R (2016) Thermal radiation heat transfer, 6th edn. CRC Press, Florida
Jacob Z (2014) Nanophotonics: hyperbolic phonon-polaritons. Nat Mater 13:1081–1083
Jacob Z, Smolyaninov II, Narimanov EE (2012) Broadband Purcell effect: radiative decay engineering with metamaterials. Appl Phys Lett 100:181105
Kane Y (1966) Numerical solution of initial boundary value problems involving maxwell's equations in isotropic media. IEEE Trans Antennas Propag 14:302–307
Khodasevych IE, Wang L, Mitchell A, Rosengarten G (2015) Micro- and nanostructured surfaces for selective solar absorption. Adv Opt Mater 3:852–881
Koppens FHL, Chang DE, García de Abajo FJ (2011) Graphene plasmonics: a platform for strong light–matter interactions. Nano Lett 11:3370–3377
Koppens FHL, Mueller T, Avouris P, Ferrari AC, Vitiello MS, Polini M (2014) Photodetectors based on graphene, other two-dimensional materials and hybrid systems. Nat Nanotechnol 9:780–793
Krishnamoorthy HNS, Jacob Z, Narimanov E, Kretzschmar I, Menon VM (2012) Topological transitions in metamaterials. Science 336:205–209
Kulkarni AP, Noone KM, Munechika K, Guyer SR, Ginger DS (2010) Plasmon-enhanced charge carrier generation in organic photovoltaic films using silver nanoprisms. Nano Lett 10:1501–1505
Kumar A, Low T, Fung KH, Avouris P, Fang NX (2015) Tunable light–matter interaction and the role of hyperbolicity in graphene–hBN system. Nano Lett 15:3172–3180
Lee BJ, Chen Y-B, Zhang ZM (2008a) Transmission enhancement through nanoscale metallic slit arrays from the visible to mid-infrared. J Comput Theor Nanosci 5:201–213
Lee BJ, Fu CJ, Zhang ZM (2005) Coherent thermal emission from one-dimensional photonic crystals. Appl Phys Lett 87:071904
Lee JH, Kim YS, Constant K, Ho KM (2007) Woodpile metallic photonic crystals fabricated by using soft lithography for tailored thermal emission. Adv Mater 19:791–794
Lee BJ, Wang LP, Zhang ZM (2008b) Coherent thermal emission by excitation of magnetic polaritons between periodic strips and a metallic film. Opt Express 16:11328–11336
Lévêque G, Martin OJF (2006) Tunable composite nanoparticle for plasmonics. Opt Lett 31:2750–2752
Li L (1996) Use of Fourier series in the analysis of discontinuous periodic structures. J Opt Soc Am A 13:1870–1876
Li L (1998) Reformulation of the fourier modal method for surface-relief gratings made with anisotropic materials. J Mod Opt 45:1313–1334

Li L (2003) Fourier modal method for crossed anisotropic gratings with arbitrary permittivity and permeability tensors. J Opt A Pure Appl Opt 5:345
Li ZQ, Henriksen EA, Jiang Z, Hao Z, Martin MC, Kim P, Stormer HL, Basov DN (2008) Dirac charge dynamics in graphene by infrared spectroscopy. Nat Phys 4:532–535
Li P, Lewin M, Kretinin AV, Caldwell JD, Novoselov KS, Taniguchi T, Watanabe K, Gaussmann F, Taubner T (2015) Hyperbolic phonon-polaritons in boron nitride for near-field optical imaging and focusing. Nat Commun 6:7507
Li W, Valentine J (2014) Metamaterial perfect absorber based hot electron photodetection. Nano Lett 14:3510–3514
Li X, Zhu J, Wei B (2016) Hybrid nanostructures of metal/two-dimensional nanomaterials for plasmon-enhanced applications. Chem Soc Rev 45:3145–3187
Lin Y, Connell JW (2012) Advances in 2D boron nitride nanostructures: nanosheets, nanoribbons, nanomeshes, and hybrids with graphene. Nanoscale 4:6908–6939
Lin C-H, Leung KM, Tamir T (2002) Modal transmission-line theory of three-dimensional periodic structures with arbitrary lattice configurations. J Opt Soc Am A 19:2005–2017
Linden S, Enkrich C, Wegener M, Zhou J, Koschny T, Soukoulis CM (2004) Magnetic response of metamaterials at 100 terahertz. Science 306:1351–1353
Ling X, Wang H, Huang S, Xia F, Dresselhaus MS (2015) The renaissance of black phosphorus. Proc Natl Acad Sci 112:4523–4530
Liu V, Fan S (2012) S4: a free electromagnetic solver for layered periodic structures. Comput Phys Commun 183:2233–2244
Liu Z, Gong Y, Zhou W, Ma L, Yu J, Idrobo JC, Jung J, MacDonald AH, Vajtai R, Lou J, Ajayan PM (2013) Ultrathin high-temperature oxidation-resistant coatings of hexagonal boron nitride. Nat Commun 4:2541
Liu R, Ji C, Mock JJ, Chin JY, Cui TJ, Smith DR (2009) Broadband ground-plane cloak. Science 323:366–369
Liu B, Liu Y, Shen S (2014) Thermal plasmonic interconnects in graphene. Phys Rev B 90:195411
Liu N, Mesch M, Weiss T, Hentschel M, Giessen H (2010) Infrared perfect absorber and its application as plasmonic sensor. Nano Lett 10:2342–2348
Liu X, Tyler T, Starr T, Starr AF, Jokerst NM, Padilla WJ (2011a) Taming the blackbody with infrared metamaterials as selective thermal emitters. Phys Rev Lett 107:045901
Liu M, Yin X, Ulin-Avila E, Geng B, Zentgraf T, Ju L, Wang F, Zhang X (2011b) A graphene-based broadband optical modulator. Nature 474:64–67
Luo C, Narayanaswamy A, Chen G, Joannopoulos JD (2004) Thermal radiation from photonic crystals: a direct calculation. Phys Rev Lett 93:213905
Marquier F, Laroche M, Carminati R, Greffet JJ (2007) Anisotropic polarized emission of a doped silicon lamellar grating. J Heat Transf 129:11–16
Mattiucci N, D'Aguanno G, Alu A, Argyropoulos C, Foreman JV, Bloemer MJ (2012) Taming the thermal emissivity of metals: a metamaterial approach. Appl Phys Lett 100:201109–201104
Messina R, Ben-Abdallah P (2013) Graphene-based photovoltaic cells for near-field thermal energy conversion. Sci Rep 3:1383
Miao X, Tongay S, Petterson MK, Berke K, Rinzler AG, Appleton BR, Hebard AF (2012) High efficiency graphene solar cells by chemical doping. Nano Lett 12:2745–2750
Mics Z, Tielrooij K-J, Parvez K, Jensen SA, Ivanov I, Feng X, Mullen K, Bonn M, Turchinovich D (2015) Thermodynamic picture of ultrafast charge transport in graphene. Nat Commun 6:7655
Modest MF (2013) Radiative heat transfer, 3rd edn. Elsevier/Academic, New York
Moharam MG, Gaylord TK (1981) Rigorous coupled-wave analysis of planar-grating diffraction. J Opt Soc Am 71:811–818
Mueller T, Xia F, Avouris P (2010) Graphene photodetectors for high-speed optical communications. Nat Photonics 4:297–301
Nagpal P, Han SE, Stein A, Norris DJ (2008) Efficient low-temperature thermophotovoltaic emitters from metallic photonic crystals. Nano Lett 8:3238–3243

Nair RR, Blake P, Grigorenko AN, Novoselov KS, Booth TJ, Stauber T, Peres NMR, Geim AK (2008) Fine structure constant defines visual transparency of graphene. Science 320:1308
Narayanaswamy A, Chen G (2004) Thermal emission control with one-dimensional metallodielectric photonic crystals. Phys Rev B 70:125101
Nefedov IS, Valagiannopoulos CA, Hashemi SM, Nefedov EI (2013) Total absorption in asymmetric hyperbolic media. Sci Rep 3:2662
Nguyen-Huu N, Chen Y-B, Lo Y-L (2012) Development of a polarization-insensitive thermophotovoltaic emitter with a binary grating. Opt Express 20:5882–5890
Nikitin AY, Guinea F, Garcia-Vidal FJ, Martin-Moreno L (2012) Surface plasmon enhanced absorption and suppressed transmission in periodic arrays of graphene ribbons. Phys Rev B 85:081405
Nikitin AY, Low T, Martin-Moreno L (2014) Anomalous reflection phase of graphene plasmons and its influence on resonators. Phys Rev B 90:041407
Novoselov KS, Geim AK, Morozov SV, Jiang D, Zhang Y, Dubonos SV, Grigorieva IV, Firsov AA (2004) Electric field effect in atomically thin carbon films. Science 306:666–669
Oskooi AF, Roundy D, Ibanescu M, Bermel P, Joannopoulos JD, Johnson SG (2010) Meep: a flexible free-software package for electromagnetic simulations by the FDTD method. Comput Phys Commun 181:687–702
Othman MAK, Guclu C, Capolino F (2013) Graphene–dielectric composite metamaterials: evolution from elliptic to hyperbolic wave vector dispersion and the transverse epsilon-near-zero condition. J Nanophotonics 7:073089–073089
Ozbay E (2006) Plasmonics: merging photonics and electronics at nanoscale dimensions. Science 311:189–193
Palik ED (1985) Handbook of optical constants of solids. Academic, San Diego
Papasimakis N, Luo Z, Shen ZX, De Angelis F, Di Fabrizio E, Nikolaenko AE, Zheludev NI (2010) Graphene in a photonic metamaterial. Opt Express 18:8353–8359
Pardo F, Bouchon P, Haïdar R, Pelouard J-L (2011) Light funneling mechanism explained by magnetoelectric interference. Phys Rev Lett 107:093902
Pendry JB (2000) Negative refraction makes a perfect lens. Phys Rev Lett 85:3966–3969
Pendry JB, Schurig D, Smith DR (2006) Controlling electromagnetic fields. Science 312:1780–1782
Piper JR, Fan S (2014) Total absorption in a graphene monolayer in the optical regime by critical coupling with a photonic crystal guided resonance. ACS Photonics 1:347–353
Poddubny A, Iorsh I, Belov P, Kivshar Y (2013) Hyperbolic metamaterials. Nat Photonics 7:948–957
Podolskiy VA, Sarychev AK, Shalaev VM (2002) Plasmon modes in metal nanowires and left-handed materials. J Nonlinear Opt Phys 11:65–74
Pop E, Varshney V, Roy AK (2012) Thermal properties of graphene: fundamentals and applications. MRS Bull 37:1273–1281
Popov E, Nevière M (2001) Maxwell equations in Fourier space: fast-converging formulation for diffraction by arbitrary shaped, periodic, anisotropic media. J Opt Soc Am A 18:2886–2894
Porto JA, García-Vidal FJ, Pendry JB (1999) Transmission resonances on metallic gratings with very narrow slits. Phys Rev Lett 83:2845–2848
Pralle MU, Moelders N, McNeal MP, Puscasu I, Greenwald AC, Daly JT, Johnson EA, George T, Choi DS, El-Kady I, Biswas R (2002) Photonic crystal enhanced narrow-band infrared emitters. Appl Phys Lett 81:4685–4687
Puscasu I, Schaich WL (2008) Narrow-band, tunable infrared emission from arrays of microstrip patches. Appl Phys Lett 92:233102–233103
Raether H (1988) Surface plasmons on smooth and rough surfaces and on gratings. Springer-Verlag, Berlin
Raman AP, Anoma MA, Zhu L, Rephaeli E, Fan S (2014) Passive radiative cooling below ambient air temperature under direct sunlight. Nature 515:540–544

Sai H, Kanamori Y, Yugami H (2003) High-temperature resistive surface grating for spectral control of thermal radiation. Appl Phys Lett 82:1685–1687
Sai H, Kanamori Y, Yugami H (2005) Tuning of the thermal radiation spectrum in the near-infrared region by metallic surface microstructures. J Micromech Microeng 15:S243
Sai H, Yugami H (2004) Thermophotovoltaic generation with selective radiators based on tungsten surface gratings. Appl Phys Lett 85:3399–3401
Sakurai A, Zhao B, Zhang Z (2014) Prediction of the resonance condition of metamaterial emitters and absorbers using LC circuit model. In: Proceedings of 15th international heat transfer conference. pp 1–10
Sakurai A, Zhao B, Zhang ZM (2015) Effect of polarization on dual-band infrared metamaterial emitters or absorbers. J Quant Spectrosc Radiat Transf 158:111–118
Schubert M (1996) Polarization-dependent optical parameters of arbitrarily anisotropic homogeneous layered systems. Phys Rev B 53:4265–4274
Schurig D, Mock JJ, Justice BJ, Cummer SA, Pendry JB, Starr AF, Smith DR (2006) Metamaterial electromagnetic cloak at microwave frequencies. Science 314:977–980
Sergeant NP, Agrawal M, Peumans P (2010) High performance solar-selective absorbers using coated sub-wavelength gratings. Opt Express 18:5525–5540
Shalaev VM, Cai W, Chettiar UK, Yuan H-K, Sarychev AK, Drachev VP, Kildishev AV (2005) Negative index of refraction in optical metamaterials. Opt Lett 30:3356–3358
Shelby RA, Smith DR, Schultz S (2001) Experimental verification of a negative index of refraction. Science 292:77–79
Smith DR, Pendry JB, Wiltshire MCK (2004) Metamaterials and negative refractive index. Science 305:788–792
Solymar L, Shamonina E (2009) Waves in metamaterials. Oxford University Press, Oxford
Song J, Si M, Cheng Q, Luo Z (2016) Two-dimensional trilayer grating with a metal/insulator/metal structure as a thermophotovoltaic emitter. Appl Opt 55:1284–1290
Srituravanich W, Fang N, Sun C, Luo Q, Zhang X (2004) Plasmonic nanolithography. Nano Lett 4:1085–1088
Stiles PL, Dieringer JA, Shah NC, Duyne RPV (2008) Surface-enhanced raman spectroscopy. Annu Rev Anal Chem 1:601–626
Strait JH, Nene P, Chan W-M, Manolatou C, Tiwari S, Rana F, Kevek JW, McEuen PL (2013) Confined plasmons in graphene microstructures: experiments and theory. Phys Rev B 87:241410
Taflove A, Hagness SC (2005) Computational electrodynamics: the finite difference time domain method, 3rd edn. Artech House, Boston
Tan Y, Liu B, Shen S, Yu Z (2016) Enhancing radiative energy transfer through thermal extraction. Nanophotonics 5:22
Thongrattanasiri S, Koppens FHL, García de Abajo FJ (2012) Complete optical absorption in periodically patterned graphene. Phys Rev Lett 108:047401
Vakil A, Engheta N (2011) Transformation optics using graphene. Science 332:1291–1294
Wang C-M, Chang Y-C, Tsai M-W, Ye Y-H, Chen C-Y, Jiang Y-W, Chang Y-T, Lee S-C, Tsai DP (2007) Reflection and emission properties of an infraredemitter. Opt Express 15:14673–14678
Wang J, Fan C, Ding P, He J, Cheng Y, Hu W, Cai G, Liang E, Xue Q (2012) Tunable broad-band perfect absorber by exciting of multiple plasmon resonances at optical frequency. Opt Express 20:14871–14878
Wang L, Haider A, Zhang Z (2014) Effect of magnetic polaritons on the radiative properties of inclined plate arrays. J Quant Spectrosc Radiat Transf 132:52–60
Wang H, Wang L (2013) Perfect selective metamaterial solar absorbers. Opt Express 21: A1078–A1093
Wang F, Wang Z, Wang Q, Wang F, Yin L, Xu K, Huang Y, He J (2015) Synthesis, properties and applications of 2D non-graphene materials. Nanotechnology 26:292001
Wang LP, Zhang ZM (2009) Resonance transmission or absorption in deep gratings explained by magnetic polaritons. Appl Phys Lett 95:111904

Wang LP, Zhang ZM (2011) Phonon-mediated magnetic polaritons in the infrared region. Opt Express 19:A126–A135
Wang LP, Zhang ZM (2012a) Measurement of coherent thermal emission by exciting magnetic polaritons in subwavelength grating structures. J Heat Transf 135:091505
Wang LP, Zhang ZM (2012b) Wavelength-selective and diffuse emitter enhanced by magnetic polaritons for thermophotovoltaics. Appl Phys Lett 100:063902
Watts CM, Liu X, Padilla WJ (2012) Metamaterial electromagnetic wave absorbers. Adv Mater 24: OP98–OP120
Williams CR, Andrews SR, Maier SA, Fernandez-Dominguez AI, Martin Moreno L, Garcia-Vidal FJ (2008) Highly confined guiding of terahertz surface plasmon polaritons on structured metal surfaces. Nat Photonics 2:175–179
Wu J, Agrawal M, Becerril HA, Bao Z, Liu Z, Chen Y, Peumans P (2009) Organic light-emitting diodes on solution-processed graphene transparent electrodes. ACS Nano 4:43–48
Xia F, Mueller T, Lin Y-m, Valdes-Garcia A, Avouris P (2009) Ultrafast graphene photodetector. Nat Nanotechnol 4:839–843
Xia F, Wang H, Xiao D, Dubey M, Ramasubramaniam A (2014) Two-dimensional material nanophotonics. Nat Photonics 8:899–907
Xuan Y (2014) An overview of micro/nanoscaled thermal radiation and its applications. Photonics Nanostruct Fundam Appl 12:93–113
Xuan Y, Zhang Y (2014) Investigation on the physical mechanism of magnetic plasmons polaritons. J Quant Spectrosc Radiat Transf 132:43–51
Yan Z, Chen L, Yoon M, Kumar S (2016) Phonon transport at the interfaces of vertically stacked graphene and hexagonal boron nitride heterostructures. Nanoscale 8:4037–4046
Yan H, Li X, Chandra B, Tulevski G, Wu Y, Freitag M, Zhu W, Avouris P, Xia F (2012) Tunable infrared plasmonic devices using graphene/insulator stacks. Nat Nanotechnol 7:330–334
Yan H, Low T, Zhu W, Wu Y, Freitag M, Li X, Guinea F, Avouris P, Xia F (2013) Damping pathways of mid-infrared plasmons in graphene nanostructures. Nat Photonics 7:394–399
Yao Y, Kats MA, Shankar R, Song Y, Kong J, Loncar M, Capasso F (2013) Wide wavelength tuning of optical antennas on graphene with nanosecond response time. Nano Lett 14:214–219
Yao Y, Shankar R, Rauter P, Song Y, Kong J, Loncar M, Capasso F (2014) High-responsivity mid-infrared graphene detectors with antenna-enhanced photocarrier generation and collection. Nano Lett 14:3749–3754
Yariv A, Yeh P (2002) Optical waves in crystals: propagation and control of laser radiation. Wiley-Interscience, New York
Yeh P (1979) Electromagnetic propagation in birefringent layered media. J Opt Soc Am 69:742–756
Yi S, Zhou M, Shi X, Gan Q, Zi J, Yu Z (2015) A multiple-resonator approach for broadband light absorption in a single layer of nanostructured graphene. Opt Express 23:10081–10090
Zayats AV, Smolyaninov II, Maradudin AA (2005) Nano-optics of surface plasmon polaritons. Phys Rep 408:131–314
Zhang ZM (2007) Nano/microscale heat transfer. McGraw-Hill, New York
Zhang ZM (2014) http://zhang-nano.gatech.edu/. Accessed 15 Aug 2016
Zhang S, Fan W, Panoiu NC, Malloy KJ, Osgood RM, Brueck SRJ (2005) Experimental demonstration of near-infrared negative-index metamaterials. Phys Rev Lett 95:137404
Zhang ZM, Fu CJ, Zhu QZ (2003) Optical and thermal radiative properties of semiconductors related to micro/nanotechnology. Adv Heat Tran 37:179–296
Zhang ZM, Wang LP (2013) Measurements and modeling of the spectral and directional radiative properties of micro/nanostructured materials. Int J Thermophys 34:2209–2242
Zhang ZM, Ye H (2012) Measurements of radiative properties of engineered micro/nanostructures. Ann Rev Heat Transf 12:345
Zhao Y, Fu C (2016) Numerical simulation on the thermal radiative properties of a 2D SiO_2/W/SiO_2/W layered grating for thermophotovoltaic applications. J Quant Spectrosc Radiat Transf 182:35–44

Zhao B, Sakurai A, Zhang ZM (2016) Polarization dependence of the reflectance and transmittance of anisotropic metamaterials. J Thermophys Heat Transf 30:240–246
Zhao B, Wang L, Shuai Y, Zhang ZM (2013) Thermophotovoltaic emitters based on a two-dimensional grating/thin-film nanostructure. Int J Heat Mass Transf 67:637–645
Zhao B, Zhang ZM (2014) Study of magnetic polaritons in deep gratings for thermal emission control. J Quant Spectrosc Radiat Transf 135:81–89
Zhao B, Zhang ZM (2015a) Strong plasmonic coupling between graphene ribbon array and metal gratings. ACS Photonics 2:1611–1618
Zhao JM, Zhang ZM (2015b) Electromagnetic energy storage and power dissipation in nanostructures. J Quant Spectrosc Radiat Transf 151:49–57
Zhao B, Zhang ZM (2017) Perfect mid-infrared absorption by hybrid phonon-plasmon polaritons in hBN/metal-grating anisotropic structures. Int J Heat Mass Transf 106:1025–1034
Zhao B, Zhao JM, Zhang ZM (2014) Enhancement of near-infrared absorption in graphene with metal gratings. Appl Phys Lett 105:031905
Zhao B, Zhao JM, Zhang ZM (2015) Resonance enhanced absorption in a graphene monolayer using deep metal gratings. J Opt Soc Am B 32:1176–1185
Zhou J, Economon EN, Koschny T, Soukoulis CM (2006) Unifying approach to left-handed material design. Opt Lett 31:3620–3622
Zhou Z, Sakr E, Sun Y, Bermel P (2016) Solar thermophotovoltaics: reshaping the solar spectrum. Nanophotonics 5:1
Zhu QZ, Lee HJ, Zhang ZM (2009) Radiative properties of materials with surface scattering or volume scattering: a review. Front Energy Power Eng China 3:60–79
Zhu L, Liu F, Lin H, Hu J, Yu Z, Wang X, Fan S (2016) Angle-selective perfect absorption with two-dimensional materials. Light: Sci Appl 5:e16052